



HAL
open science

A simple and efficient control allocation scheme for on-ground aircraft runway centerline tracking

Edouard Sadien, Clément Roos, Abderazik Birouche, Mathieu Carton, Christophe Grimault, Louis Emmanuel Romana, Michel Basset

► **To cite this version:**

Edouard Sadien, Clément Roos, Abderazik Birouche, Mathieu Carton, Christophe Grimault, et al.. A simple and efficient control allocation scheme for on-ground aircraft runway centerline tracking. *Control Engineering Practice*, 2020, 95, pp.104228. 10.1016/j.conengprac.2019.104228 . hal-02902600

HAL Id: hal-02902600

<https://hal.science/hal-02902600>

Submitted on 20 Jul 2020

HAL is a multi-disciplinary open access archive for the deposit and dissemination of scientific research documents, whether they are published or not. The documents may come from teaching and research institutions in France or abroad, or from public or private research centers.

L'archive ouverte pluridisciplinaire **HAL**, est destinée au dépôt et à la diffusion de documents scientifiques de niveau recherche, publiés ou non, émanant des établissements d'enseignement et de recherche français ou étrangers, des laboratoires publics ou privés.

A simple and efficient control allocation scheme for on-ground aircraft runway centerline tracking

Edouard Sadien¹, Clément Roos^{2,*}, Abderazik Birouche³, Mathieu Carton¹,
Christophe Grimault¹, Louis Emmanuel Romana¹ and Basset³

¹ Airbus Operations S.A.S., Toulouse, France

² ONERA, The French Aerospace Lab, Toulouse, France

³ IRIMAS, Université de Haute-Alsace, Mulhouse, France

* Corresponding author: clement.roos@onera.fr

Abstract

To achieve a high performance level during ground operations, the lateral dynamics of an aircraft must be controlled using all available actuators (rudder, nose-wheel steering system, engines and brakes) and under various constraints, which gives rise to a challenging allocation problem. To address this issue, a simple yet accurate design-oriented on-ground aircraft model is first developed. It takes into account the effects of aerodynamics, thrust and tire-ground interactions, both laterally and longitudinally, and for several runway states. It is validated on a high-fidelity Airbus simulator and a complete set of numerical values representative of a commercial aircraft is given, as well as design objectives, so as to provide the control community with a challenging benchmark. After an extensive literature review and an evaluation of the pros and cons of many existing control allocation techniques, a novel and easily implementable algorithm is then developed, which meets actuator and implementation constraints. It automatically manages the trade-off between two antagonistic objectives, namely minimizing the control effort and attaining the maximum virtual control. Its validation on both the design-oriented model and the high-fidelity simulator shows promising results.

Keywords: on-ground aircraft modeling, ground control architecture, control allocation, Monte Carlo-based validation.

1 Introduction

Many airborne phases of commercial flights have been automated with the development of fly-by-wire solutions [1]. However, after touchdown, the motion of the aircraft is usually controlled manually by the pilot using throttle levers, rudder pedals, tillers and brake pedals. This is especially demanding in adverse conditions such as contaminated runways and severe crosswinds. Following a study carried out by the International Civil Aviation Organization, the count of runway excursions has not decreased over the last 20 years

[2]. The main factors, analyzed in [3], are mainly due to wet/contaminated runways, crosswinds and nose-wheel steering (NWS) problems. Nevertheless, automation is possible under constraining ground infrastructure and operational requirements.

Therefore, there is a strong motivation to develop enhanced control allocation algorithms able to manage multiple devices with different characteristics. But at present, solutions are rare and often only partial. Several design strategies have been proposed to control the aircraft using the NWS system only, or less frequently with the rudder as well (see *e.g.* [4, 5, 6]). A lot of progress has also been made in the longitudinal energy management and control [7, 8], such as the Brake To Vacate function developed by Airbus [9]. But one of the most challenging on-ground control problems – which currently lacks a satisfactory solution – occurs at intermediate speed between 40 and 80 knots (kt), where the rudder and the NWS system are less efficient. The main objective is to ensure that the lateral deviation with respect to the runway centerline remains acceptable despite wind, varying runway state and comfort constraints. Achieving good performance during this worst-case scenario makes it necessary to use differential braking in addition to classical control devices (rudder and NWS system). But on the other hand, brakes should only be used sparingly to avoid a deterioration in braking performance and an increase in ground holding time for maintenance or cooling purposes.

In this context, the contribution of this paper is threefold. An accurate on-ground aircraft model of tractable complexity is first developed to address various control issues such as runway centerline tracking. A thorough comparison of the most relevant control allocation techniques (see *e.g.* [10, 11]) is then presented, based on a realistic worst-case landing scenario initially proposed in [12]. A novel allocation technique is finally introduced to solve the aforementioned allocation problem. It takes advantage of the implementation ease of the pseudo-inverse, smartly manages the trade-off between minimizing actuators use and attaining maximum virtual control, and allows the simultaneous saturation of the actuators, which is desirable for efficient failure recovery. The proposed aircraft model and allocation technique are both validated on a high-fidelity Airbus simulator by means of intensive Monte Carlo type simulations.

The paper is organized as follows. The control objectives are stated in Section 2. The on-ground aircraft model is thoroughly described in Section 3 and an overview of the whole control architecture is briefly presented in Section 4. Section 5 is devoted to the control allocation review, and the novel algorithm is developed in Section 6. Detailed numerical results are finally presented in Section 7.

2 Control Objectives

The main objective is to develop a control architecture for the lateral control of an on-ground aircraft, which minimizes the lateral deviation with respect to the runway centerline during the deceleration phase despite external disturbances such as wind and varying runway state. Currently implemented solutions only make use of the rudder and the NWS system. In order to use both actuators efficiently, it is desirable that they reach saturation almost simultaneously to allow efficient recovery in case of failure. Indeed, having a failed actuator at maximum deflection and the other one at smaller deflection requires more time to recover, which can be critical.

Moreover, there is a need to extend the operational domain, taking into account demanding scenarios and failure cases through the smart use of differential braking. Regulations require aircraft brakes to be able to handle a rejected or aborted takeoff at any moment prior to the plane reaching a decision speed. To make this possible, the brakes should not exceed a specified temperature before engaging a takeoff, so as to avoid a subsequent performance degradation or a fire breakout in the main landing gear bays. Moreover, research has shown that the number of brake applications contributes more to carbon brake wear than the intensity of each application [13]. So the minimization of differential braking is a strong industrial requirement to reduce the likelihood of brake wear and overheating, and therefore delayed departures. This is of utmost importance after ensuring the safety of the aircraft.

3 Aircraft Modeling

Most existing design-oriented on-ground aircraft models only focus on the lateral behavior [5, 14, 6]. A few others consider both the lateral and the longitudinal motions, but the coupling effects due to the tire-road interactions are either not discussed or incomplete [15, 16, 17, 14]. Moreover, the operational domain is often limited to taxiing [5], and if higher speed is considered, only the rudder is usually taken into account in addition to the NWS system [15, 6].

To go one step further and take into account the constraints set out in Section 2, a 3 degree-of-freedom (DOF) model was recently introduced in [18]. Both the longitudinal and lateral aerodynamic effects and the tire-ground interactions are included, as well as simple dependencies on the vertical load and the runway state. Moreover, all actuators of interest (NWS system, rudder, engines and brakes) are modeled, including their dynamics and limitations. An intensive validation process revealed that this model is usually very accurate, except when the anti-skid system is active, in which case the proposed pseudo-decoupling of the ground forces is arguable. To

address this issue, this paper improves the work of [18] by introducing a better model of the coupled longitudinal and lateral ground forces, at the price of a very reasonable increase in complexity.

3.1 Simplifying Assumptions and General Equations

The model described here is representative of an aircraft on the ground during the roll-out phase, where the objective is to decelerate while keeping a straight trajectory on the runway. The following assumptions are made to simplify the general nonlinear equations of motion recalled in [18], yielding a model of tractable complexity adapted for control design:

- (A1) Tricycle configuration.
- (A2) Planar motion, *i.e.* negligible roll, pitch and vertical speed.
- (A3) Small tire sideslip and nose-wheel deflection angles, thus setting a speed lower bound of 40 kt.
- (A4) Linearized expressions for the aerodynamic effects, implying a small aerodynamic sideslip angle and a maximum crosswind of 10 kt in the $\vec{x}_b\vec{y}_b$ plane (see Figure 1), and setting a speed upper bound of 100 kt.
- (A5) Velocity of each main landing gear wheels center equal to that of its normal projection on the aircraft plane of symmetry.
- (A6) Forward engines thrust (no reverse) aligned with the fuselage axis \vec{x}_b .

Most commercial aircraft have three landing gears. Moreover, all tires of a given landing gear experience roughly the same normal load, sideslip angle, braking torque and runway state. Thus, they can reasonably be reduced to a single point, which validates (A1). Then, most runways being relatively flat, the aircraft and the shock absorbers being highly rigid, and this paper focusing on runway centerline tracking (no strong lateral maneuvers), the aircraft motion can be considered as planar, as assumed in (A2). During roll-out, the aircraft leaves the runway at around 40 kt, which justifies the lower bound on the longitudinal velocity V_x in (A3). In practice, while on the runway, the lateral velocity and the yaw rate do not exceed $V_{yMAX} = 1$ m/s and $r_{MAX} = 10$ deg/s respectively. Moreover, the nose-wheel deflection θ_{NW} is typically below 6 deg to prevent breakage. Consequently, the tire sideslip angles attain a maximum value of roughly 5 deg as can be checked with (7a) and (7b), which completely validates (A3). Using linearized expressions for the aerodynamic effects is a common practice given that the aerodynamic configuration is fixed and the aerodynamic sideslip angle β remains small enough, typically below 17 deg for the considered application. Given the aforementioned bounds on V_x and V_y , this leads to a maximum horizontal crosswind of 10 kt. Furthermore, the ground spoilers being deployed at around 100 kt, this sets an upper bound on V_x , which concludes the justification of (A4). Then, it can be checked that rDy_{MG} is at most equal to 3% of V_x and can be neglected in the denominator of (7b), thus leading to the same expression for the left and right tire sideslip angles, and

validating (A5). Finally, reversers are not considered here as this would affect the aerodynamic model due to the modified airflow on the aerodynamic surfaces. Furthermore, on commercial aircraft, the orientation difference between the thrust direction and the fuselage axis is negligible, hence justifying (A6).

Remark 1. *These assumptions remain valid during the take-off phase, and the speed range can even be increased. The model is indeed accurate as soon as the aircraft is aligned on the runway up to the take-off speed since the aerodynamic configuration remains constant.*

Remark 2. *The validity domain of the model may seem narrow, particularly concerning the wind disturbance. In reality, the bound of 10 kt introduced in (A4) is tight when $V_x = 40$ kt but could be increased linearly with V_x to reach a value of 30 kt at $V_x = 100$ kt, so (A4) could be slightly alleviated. Anyway, the control laws developed under the proposed assumptions perform very well on a much wider operational domain, as shown in Subsection 7.3.*

Thanks to assumption (A2), the 3 DOF body motion can be described

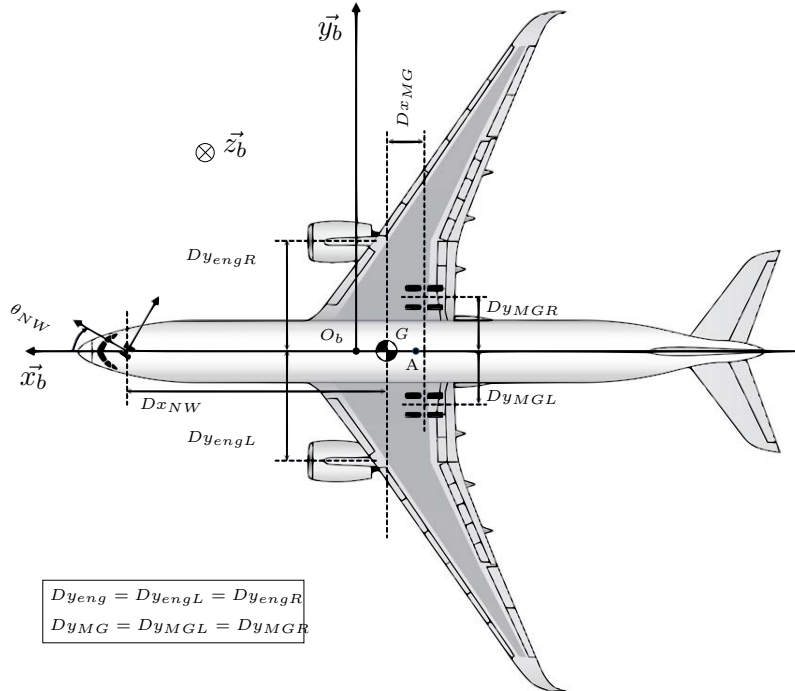


Figure 1: Body reference system \mathcal{R}_b and aircraft geometry

in the reference system \mathcal{R}_b by:

$$\begin{aligned}\dot{V}_x &= F_x/m + r V_y \\ \dot{V}_y &= F_y/m - r V_x \\ \dot{r} &= M_r/I_{zz} \\ \dot{\psi} &= r\end{aligned}\quad (1)$$

where V_x, V_y, r, m, I_{zz} and ψ are the longitudinal and lateral velocities, the yaw rate, the aircraft mass, the inertia around the \vec{z}_b axis, and the aircraft heading respectively. There is no roll and pitch, so the weight does not appear in (1). Therefore, the longitudinal and lateral forces $F_x = \Sigma F_{xi}$ and $F_y = \Sigma F_{yi}$, and the yawing moment $M_r = \Sigma M_{ri}$, are each written as the sum of 3 terms, where i denotes engines thrust (*eng*), aerodynamic effects (*a*) or ground reaction (*g*).

According to (A6), the engines thrust and moment can be expressed as follows:

$$\begin{aligned}F_{xeng} &= T_{engL} + T_{engR} \\ F_{yeng} &= 0 \\ M_{reng} &= Dy_{eng}(T_{engL} - T_{engR})\end{aligned}\quad (2)$$

where T_{engL}, T_{engR} and Dy_{eng} denote the thrust of the left and right engines, and the lateral distance between the center of gravity G and the engines respectively.

The aerodynamic velocity \vec{V}_a in \mathcal{R}_b is defined as:

$$\vec{V}_a = \vec{V} - \vec{W} = [V_{ax} \ V_{ay} \ 0]^T \quad (3)$$

since the wind disturbance $\vec{W} = [W_x \ W_y \ 0]^T$ is in the $\vec{x}_b\vec{y}_b$ plane and $\vec{V} = [V_x \ V_y \ 0]^T$ according to assumptions (A4) and (A2) respectively. Assumption (A4) then allows to considered linearized aerodynamic effects at the aerodynamic center A [19]:

$$\begin{aligned}F_{xa} &= q_d S C x_0 \\ F_{ya} &= q_d S \left(C y_\beta \beta + C y_r \frac{r c}{V_a} + C y_{\delta r} \delta r \right) \\ M_{ra} &= q_d S c \left(C n_\beta \beta + C n_r \frac{r c}{V_a} + C n_{\delta r} \delta r \right) \\ F_{za} &= q_d S C z_0\end{aligned}\quad (4)$$

where V_a is the Euclidean norm of \vec{V}_a , while $q_d = \frac{1}{2}\rho V_a^2$ and S are the dynamic pressure and the reference surface respectively. In addition, Cx_0, Cy_j, Cn_j and Cz_0 refer to the drag, lateral, yaw and lift stability derivatives, and j denotes the effect due to the aerodynamic sideslip angle $\beta = \arctan(V_{ay}/V_{ax})$ (approximated by V_{ay}/V_{ax} under assumption (A4)), the yaw rate r or the rudder deflection δr . Note that the angle of attack is zero

since $V_z = W_z = V_{az} = 0$, which explains why the drag and lift coefficients are constant.

Finally, the ground reaction model is significantly more complicated and is detailed in Section 3.2 below.

3.2 Contact Force Model

As shown in Figure 2b, a tire in motion is subject to normal reaction F_{z_k} , rolling resistance F_{r_k} and slip forces F_{sx_k} and F_{sy_k} , the latter arising from the presence of longitudinal and lateral slip between the contact patch and the ground. These forces act at the points P_k and are expressed in the wheel reference systems \mathcal{R}_k , where k refers to the nose-wheel (*NW*) or the left (resp. right) main landing gear (*MGL* (resp. *MGR*)), according to assumption (A1). Note that the nose-wheel is a free rolling wheel (*i.e.* neither driven nor braked), so the longitudinal slip force $F_{sx_{NW}}$ is equal to 0.

Normal Reaction The forces F_{r_k} , F_{sx_k} and F_{sy_k} depend on the normal reaction F_{z_k} . Thanks to assumption (A2), the latter is the same for both main landing gears. Therefore, moment balances around the \vec{y}_b axis at the nose and main landing gear wheels yield:

$$\begin{aligned} F_{z_{NW}} &= \frac{m g D x_{MG} - F_{za} (D x_{MG} - c (c_A - c_G))}{D x_{NW} + D x_{MG}} \\ F_{z_{MGR}} = F_{z_{MGL}} &= \frac{1}{2} \frac{m g D x_{NW} - F_{za} (D x_{NW} + c (c_A - c_G))}{D x_{NW} + D x_{MG}} \end{aligned} \quad (5)$$

where $D x_{NW}$ and $D x_{MG}$ are positive distances shown in Figure 1, and g is the standard gravity. The origin O_b of \mathcal{R}_b is chosen to be the start position of the mean aerodynamic chord c . Thus, the weight and the aerodynamic effects act at the points G and A located along \vec{x}_b respectively, whose x-coordinates are $X_G = -c_G c$ and $X_A = -c_A c$, c_G and c_A being positive dimensionless coefficients. Note that the normal reaction forces are defined positive along the $-\vec{z}_b$ axis.

Rolling Resistance Rolling resistance arises due to the hysteresis of rubber during deformation of the tire and is considered as proportional to F_{z_k} . Other models exist where the rolling friction coefficient μ_r is function of powers of the longitudinal speed [20, 21], pressure and other parameters, but they are not considered here for the sake of simplicity. In this study, the rolling resistance F_{r_k} is indeed negligible compared to the thrust and braking forces during take-off and roll-out respectively. It acts backwards along the $-\vec{x}_k$ axis as shown in Figure 2b and is given by:

$$F_{r_k} = \mu_r F_{z_k} \quad (6)$$

where $\mu_r = \bar{\mu}\mu_{rMAX}$ depends on the characteristics of the surface in contact with the wheels. The relative friction coefficient $\bar{\mu}$ depends on the runway state. It is typically equal to 1 for dry, 0.74 for wet and 0.29 for snowy runways. μ_{rMAX} is the maximum rolling friction coefficient for a dry runway.

Tire Sideslip Angles The lateral slip forces F_{sy_k} do not only depend on normal reaction, but they are also function of the tire sideslip angles β_k , which can be computed as in [22]:

$$\beta_{NW} \underset{(A3)}{=} \frac{V_y + r Dx_{NW}}{V_x} - \theta_{NW} \quad (7a)$$

$$\beta_{MGR} \underset{(A5)}{=} \beta_{MGL} \underset{(A5)}{=} \beta_{MG} \underset{(A3)}{=} \frac{V_y - r Dx_{MG}}{V_x} \quad (7b)$$

In contrast to [18], β_{MGR} and β_{MGL} are no longer equal to $\beta_G = V_y/V_x$, which improves accuracy for large aircraft.

Contact Force Model A simplified lateral slip force model is proposed in [15]:

$$F_{sy_k} = - N_{t_k} \text{sat}_{[\bar{\mu} F_{syMAX_k}]}(G_{y_k} \beta_k) \quad (8)$$

where the saturation operator is defined as $\text{sat}_{[F]}(x) = x$ if $|x| < F$ and $\text{sat}_{[F]}(x) = F$ otherwise, and the saturation level $\bar{\mu} F_{syMAX_k}$ depends on the runway state and the maximum lateral force F_{syMAX_k} (for a dry runway). N_{t_k} denotes the number of tires, and the cornering gain $G_{y_k} = \left. \frac{\partial F_{sy_k}}{\partial \beta_k} \right|_{\beta_k=0}$ is computed for a mean value of the normal reaction. No explicit dependency of G_{y_k} on F_{z_k} is considered in [15], but an uncertainty is introduced on G_{y_k} , whose bounds are determined thanks to extensive simulations. This is illustrated in Figure 3, where the nominal model (8) is shown by the green dashed line, while the bounds on the uncertain cornering gain are displayed by the brown dot-dashed lines.

Based on [15], an improved model is proposed in this paper, which accounts for combined slip, runway state and normal load variation. The combined longitudinal and lateral slip force $F_{s_k} = \sqrt{F_{sx_k}^2 + F_{sy_k}^2}$ generated by an isotropic tire, under non-zero longitudinal slip and sideslip, cannot exceed μF_{z_k} [23], where $\mu = \bar{\mu}\mu_{MAX}$ denotes the tire-road friction coefficient and μ_{MAX} its maximum value (corresponding to a dry runway). Therefore, the maximum force boundary can be represented by the orange circle in Figure 2a. But the considered operational conditions allow to simplify this coupling between F_{sx_k} and F_{sy_k} . Indeed, the sideslip angle β_k remains small during the roll-out phase, typically less than 5 degrees in practice. Moreover, the anti-skid system ensures that the longitudinal slip force does not

exceed $\eta_{AS}\mu F_{z_k}$, where η_{AS} denotes the anti-skid efficiency. In other words, it prevents the longitudinal slip ratio from becoming too large, and the optimal slip corresponding to the maximum longitudinal slip force cannot be reached. In this context, it can be reasonably assumed that the resultant of the slip forces lies inside the orange area instead of the orange circle in Figure 2a, where the longitudinal and lateral maximum forces are represented in green and blue respectively. The following model is then assumed:

$$F_{sx_k} = \text{sat}[\eta_{AS}\bar{\mu}\mu_{MAX}F_{z_k}] \left(\frac{N_{t_k} T_{brk_k}}{R_e} \right) \quad (9)$$

$$F_{sy_k} = -\sqrt{(\bar{\mu}\mu_{MAX}F_{z_k})^2 - F_{sx_k}^2} \tanh\left(\frac{K_{y_k}\beta_k}{\bar{\mu}\mu_{MAX}}\right) \quad (10)$$

where R_e and T_{brk_k} correspond to the wheel effective radius and the braking torque respectively (see Figure 2b), and K_{y_k} is the reduced lateral cornering gain. The latter is independent of speed in the operational domain but depends on the runway state according to [24]:

$$K_{y_k} = \frac{K_{yMAX_k}}{\frac{2}{3} + \frac{1}{3\bar{\mu}}} \quad (11)$$

where K_{yMAX_k} denotes the reduced lateral cornering gain defined for a dry runway.

Remark 3. *Under a fixed braking torque, F_{sx_k} should remain constant as long as V_x is not null and the wheels keep rolling [20], which is the case in (9). Moreover, F_{sx_k} should normally increase in a relatively linear way, reach a maximum value F_{sxMAX_k} and then decrease as T_{brk_k} increases. But the anti-skid prevents the lock of the wheels and F_{sxMAX_k} is never reached in practice. Therefore, the proposed model is accurate enough.*

Remark 4. *A first attempt to improve [15] was done in [18]: (a) a more realistic longitudinal model was developed, (b) a pseudo-coupling between the longitudinal and lateral forces was also proposed, whereas an a priori decoupling was performed in [15] and finally, (c) the normal load and the runway state were explicitly considered in the cornering gain and the saturation levels. The model in [18] is usually accurate, except during the anti-skid system activation, where the pseudo-decoupling is arguable. This is why further improvements are introduced in this paper: a more precise saturation value based on the anti-skid system limitation for the longitudinal force, a more precise time-varying longitudinal-lateral ground forces coupling, and an approximation of the lateral force by the sigmoid function \tanh , which leads to a smoother and more realistic behavior than the saturation function used in [15] and [18]. To sum up, [18] can be seen as an intermediate result between [15] and the model proposed in (9) and (10). The latter is quite accurate up to moderate values of the slip angle β_k , which is the case*

in the considered operational domain, even in the presence of combined slip. Therefore, the admissible tire forces, defined by the orange area in Figure 2a, now spans a larger area than in [18].

Under assumption (A3), $\sin \theta_{NW}$ and $\cos \theta_{NW}$ can be replaced with θ_{NW} and 1 respectively. The total contact forces and moments at G are thus given in \mathcal{R}_b by:

$$F_{xg} = -F_{r_{NW}} - F_{r_{MGR}} - F_{r_{MGL}} - F_{sy_{NW}} \theta_{NW} - F_{sx_{MGR}} - F_{sx_{MGL}} \quad (12a)$$

$$F_{yg} = -F_{r_{NW}} \theta_{NW} + F_{sy_{NW}} + F_{sy_{MGR}} + F_{sy_{MGL}} \quad (12b)$$

$$M_{rg} = (F_{sy_{NW}} - F_{r_{NW}} \theta_{NW}) Dx_{NW} - (F_{sy_{MGR}} + F_{sy_{MGL}}) Dx_{MG} \\ + (F_{sx_{MGR}} + F_{r_{MGR}}) Dy_{MG} - (F_{sx_{MGL}} + F_{r_{MGL}}) Dy_{MG} \quad (12c)$$

where Dy_{MG} denotes the lateral distance between G and the main landing gears.

3.3 Actuators and Engines Models

Each engine is considered as quasi-static and approximated by a first order dynamic model of nominal gain T_{engMAX} and time constant τ_{eng} , with position and rate limits $L_{peng} = [N_{1IDLE}, N_{1MAX}]$ and L_{reng} [25]. The position limit is due to mechanical stops of the throttle, further limited by the operational domain between the Idle Forward and Take Off Go Around positions:

$$\tau_{eng} \dot{N}_{1k} + N_{1k} = N_{1k_c} \quad \text{with} \quad \begin{cases} N_{1k} \in L_{peng} \\ |\dot{N}_{1k}| \leq L_{reng} \end{cases} \quad (13a)$$

$$T_{eng_k} = N_{1k} T_{engMAX} \quad (13b)$$

where N_{1k} and N_{1k_c} are the actual and the commanded engine throttle settings respectively, and $k \in \{L, R\}$. In contrast to [18], asymmetric thrust is now considered and the engines are commanded through throttle levers.

Each braking system is approximated by a first order dynamic model of nominal gain G_{brk} and time constant τ_{brk} , with position and rate limits L_{pbrk} and L_{rbrk} :

$$\tau_{brk} \dot{P}_{brk_k} + P_{brk_k} = P_{brk_k_c} \quad \text{with} \quad \begin{cases} 0 \leq P_{brk_k} \leq L_{pbrk} \\ |\dot{P}_{brk_k}| \leq L_{rbrk} \end{cases} \quad (14)$$

where P_{brk_k} and $P_{brk_k_c}$ are the actual and the commanded braking pressures respectively, and $k \in \{MGL, MGR\}$. Braking starts only if P_{brk_k} is

above a threshold P_0 , so as to overcome the restoring force of springs located between the brake discs and pistons. The produced braking torques are thus obtained as:

$$T_{brk_k} = \max(0, G_{brk}(P_{brk_k} - P_0)) \quad (15)$$

The NWS (resp. the rudder) actuation system is approximated by a first order dynamic model of unit gain and time constant τ_{NW} (resp. $\tau_{\delta r}$), with position and rate limits L_{pNW} and L_{rNW} (resp. $L_{p\delta r}$ and $L_{r\delta r}$):

$$\tau_{NW}\dot{\theta}_{NW} + \theta_{NW} = \theta_{NW_c} \quad \text{with} \quad \begin{cases} |\theta_{NW}| \leq L_{pNW} \\ |\dot{\theta}_{NW}| \leq L_{rNW} \end{cases} \quad (16)$$

$$\tau_{\delta r}\dot{\delta r} + \delta r = \delta r_c \quad \text{with} \quad \begin{cases} |\delta r| \leq L_{p\delta r} \\ |\dot{\delta r}| \leq L_{r\delta r} \end{cases} \quad (17)$$

where θ_{NW} and θ_{NW_c} (resp. δr and δr_c) are the actual and the commanded nose-wheel (resp. rudder) deflections.

3.4 Model Summary

The entire model structure is shown in Figure 4a. The *Actuators* block contains the engine models, as well as the NWS, braking and rudder actuator models. The thrust, the aerodynamic effects and the contact forces are computed in the *Forces & Moments* block, whose structure is detailed in Figure 4b. To sum up, the model is composed of:

- 6 control inputs $N_{1L_c}, N_{1R_c}, P_{brk_{MGL_c}}, P_{brk_{MGR_c}}, \theta_{NW_c}, \delta r_c$,
- 2 wind disturbances $\vec{W} = [W_x \ W_y \ 0]^T$,
- the runway relative friction coefficient $\bar{\mu}$,
- 4 aircraft states (V_x, V_y, r, ψ) and 6 actuator states,
- 8 measured outputs $V_x, V_y, r, \psi, \dot{r}, \theta_{NW}$, longitudinal and lateral load factors $N_x = -\frac{\dot{V}_x - r V_y}{g}$ and $N_y = -\frac{\dot{V}_y + r V_x}{g}$, which can be used by the control laws.

Each sensor is represented by a first order filter of unit gain and time constant τ_{sensor} , and a delay τ_{delay} . A complete set of numerical values representative of a commercial aircraft is provided in Table 1. Some of these values are not known accurately, therefore a $\pm 10\%$ uncertainty on the stability derivatives, the cornering gains, and the runway state (impacted by badly known external conditions), can be considered.

Parameter	Unit	Typical value
m	kg	60×10^3
I_{zz}	kg.m ²	3.70×10^6
S	m ²	122
c	m	4.2
c_G / c_A	-	0.30 / 0.42
$Dx_{NW} / Dx_{MG} / Dy_{MG}$	m	11.45 / 1.19 / 3.80
Cx_0 / Cz_0	-	-0.090 / 0.905
Cy_β / Cn_β	-	-1.36 / 2.50
Cy_r / Cn_r	-	3.69 / -16.29
$Cy_{\delta r} / Cn_{\delta r}$	-	0.34 / -2.01
μ_{rMAX} / μ_{MAX}	-	0.015 / 0.68
K_{yMAXNW} / K_{yMAXMG}	/rad	3.56 / 3.49
R_e	m	0.50
η_{AS}	-	0.95
$N_{tNW} = N_{tMGL} = N_{tMGR} = N_{tMG}$	-	2
$\tau_{sensor} / \tau_{delay}$	s	$1 \times 10^{-3} / 5 \times 10^{-2}$
$\tau_{eng} / \tau_{brk} / \tau_{NW} / \tau_{\delta r}$	s	$2 / 10^{-3} / 0.5 / 0.2$
N_{1IDLE} / N_{1MAX}	%	18 / 100
T_{engMAX}	N	150×10^3
$L_{pbrk} / P_0 / L_{pbrkCA}$	bar	175 / 15 / 30
L_{rbrk}	Pa/s	20×10^5
G_{brk}	Nm/Pa	4×10^{-3}
$L_{pNW} / L_{p\delta r} / L_{pNWC_A} / L_{p\delta rCA}$	deg	74 / 30 / 6 / 30
$L_{rNW} / L_{r\delta r}$	deg/s	20 / 30

Table 1: Typical numerical values for a commercial aircraft

3.5 Model Validation

The proposed model is compared to a high-fidelity Airbus simulator in order to assess the effectiveness of the contact force and actuators models. The simulator has been developed for control laws validation purposes [26] and is valid in the whole flight domain. Its inputs are sent through the cockpit control organs and the corresponding actuators orders are obtained by kinematic relationships. These orders are then sent to the proposed aircraft model. Furthermore, the linearized aerodynamic model has already been validated in various studies [15, 4, 27] and is not validated again here: the simulator aerodynamic forces and moments F_{xa}, F_{ya}, M_{ra} are directly fed into the model.

The nose-wheel efficiency increases as the normal load on the tires becomes larger, *i.e.* at low speed. On the opposite, the rudder efficiency increases as the aerodynamic effects become larger, *i.e.* at high speed. And differential braking is interesting at medium speed (between 40 and 80 kt)

to compensate for the reduced efficiency of the classical actuators. Moreover, the influence of slip forces strongly depends on the runway state, so the nose-wheel behavior should also be validated on a low friction runway. In this context, the three following maneuvers are considered to cover as much as possible the entire operational domain. They correspond to usual pilot actions during the roll-out phase with the engines at idle:

- *Maneuver 1*: ± 2 deg trapezoidal-doublet of the rudder pedal deflection on a dry runway between 100 and 70 kt,
- *Maneuver 2*: right then left 3 deg trapezoidal brake pedal deflection on a wet runway between 80 and 50 kt,
- *Maneuver 3*: ± 4 deg trapezoidal-doublet of the hand-wheel on a snowy runway between 60 and 40 kt.

Maneuver 2 is the one for which the differences between the simulator and the model are the greatest. The associated time responses are shown in Figure 5, where the vertical axes are normalized since they contain Airbus proprietary data. The other maneuvers are shown in Appendix. A fitting ratio between the simulator and the model is also calculated for each curve and its minimum (*i.e.* worst) value for each of the three maneuvers is given in Table 2:

$$\text{Fitting ratio (\%)} = \left(1 - \frac{\int (y_{sim} - y_{model})^2 dt}{\int (y_{sim})^2 dt} \right) \times 100 \quad (18)$$

	Maneuver 1 (high speed)	Maneuver 2 (medium speed)	Maneuver 3 (low speed)
Minimum fitting ratio	91.59%	90.25%	93.90%

Table 2: Minimum fitting ratio for each maneuver

The lateral behavior of the proposed model is close to that of the high-fidelity Airbus simulator over the entire operational domain. The main differences in Figures 5, 13 and 14 are in the peak values, but they remain quite reasonable. Hence, the proposed model is sufficiently representative of the true aircraft to design ground control laws in the next sections.

4 Control Architecture Overview

Figure 6 shows the whole lateral ground control architecture. A body-axis yaw rate command r_c is first computed by the outer-loop guidance law \mathbf{G} to minimize the aircraft lateral deviation despite wind disturbances \vec{W} and

varying runway state $\bar{\mu}$. It can also be sent directly by the pilot based on his perception of the aircraft motion. The inner-loop control law **NDI** then generates a virtual yaw acceleration command \dot{r}_{act_c} to be produced by the actuators via the control allocation module **CA**. The latter finally outputs the commanded actuator deflections and interacts with the longitudinal controller K_L for the brakes management.

Guidance Law The guidance law (**G block**) is given by:

$$r_c = K_Y (Y_0 - Y_c) + K_{V_y} V_{y0} + K_{A_y} A_{y0} \quad (19)$$

where Y_c , Y_0 , V_{y0} and A_{y0} denote respectively the reference lateral distance from the runway centerline (equal to zero here), and the actual lateral distance, velocity and acceleration in the runway reference system, given by the navigation system (**Nav block**). In practice, the transfer function between Y_c and Y_0 is first computed. To do so, V_{y0} and A_{y0} are replaced in the Laplace domain with sY_0 and s^2Y_0 respectively, r_c is replaced with the yaw rate r as shown in (24), and r is finally connected to Y_0 as follows:

$$s^2Y_0 = \frac{V_x}{1 + \tau_y s} r \quad (20)$$

Equation (20) is obtained by setting $\dot{V}_y = 0$ in (1), *i.e.* by assuming that the system has reached the steady state. F_y/m is then approximated by A_{y0} , which leads to $s^2Y_0 = r V_x$, and the transient phase is considered approximately by adding a first order filter with time constant τ_y . The gains K_Y , K_{V_y} and K_{A_y} are finally computed by a modal approach so that the transfer between Y_c and Y_0 is well-damped and sufficiently fast.

Yaw Rate Control Law The yaw angular acceleration can be written as the sum of a control-independent acceleration \dot{r}_B and a control-dependent acceleration \dot{r}_{act} :

$$\dot{r} = \dot{r}_B + \dot{r}_{act} \quad (21)$$

The term \dot{r}_B includes the coupling between the lateral and longitudinal tire forces, which allows the Yaw Rate Control Law to adapt to the longitudinal behavior of the aircraft. Using a nonlinear dynamic inversion based approach [28], the closed-loop dynamics are imposed by forcing \dot{r} to be equal to a desired value \dot{r}_M . This yields the following control law:

$$\dot{r}_{act_c} = \dot{r}_M - \dot{r}_B \quad (22)$$

$$\dot{r}_M = k_d r_c + k_i \int (r_c - r) + k_r r \quad (23)$$

implemented in the **NDI block**, where the desired yaw rate r_c is determined by the guidance law or sent by the pilot. After a few manipulations, the

following transfer function between r_c and r is obtained:

$$\frac{r}{r_c} = \frac{(1 + \tau_r s) \omega_r^2}{s^2 + 2\xi_r \omega_r s + \omega_r^2} \quad (24)$$

where the frequency ω_r , the damping ξ_r and the time constant τ_r depend on the gains k_d , k_i and k_r . The latter are finally tuned so that the closed-loop system is fast and well-damped.

Control Allocator The number of control effectors being greater than the number of controlled variables, an allocation algorithm (**CA block**) is required to distribute \dot{r}_{act_c} among the redundant set of actuators. It produces the commanded nose-wheel and rudder deflections θ_{NW_c} and δr_c , and the difference $\delta P_{brk_c} = P_{brk_{MGR_c}} - P_{brk_{MGL_c}}$ between the right and left braking pressures.

Longitudinal Motion Management During the roll-out phase, the longitudinal motion manager (K_L **block**) computes the commanded left and right braking pressures $P_{brk_{MGL_c}}$ and $P_{brk_{MGR_c}}$ based on the pilot mean braking pressure command $P_{brk_{COM_c}}$ and the pressure difference δP_{brk_c} provided by the allocator:

$$\begin{aligned} P_{brk_{MGL_c}} &= P_{brk_{COM_c}} - 0.5\delta P_{brk_c} \\ P_{brk_{MGR_c}} &= P_{brk_{COM_c}} + 0.5\delta P_{brk_c} \end{aligned} \quad (25)$$

A controller could be designed to adjust $P_{brk_{COM_c}}$, so as to ensure that the aircraft stops at a certain distance on the runway while respecting deceleration constraints (see *e.g.* the Brake To Vacate function developed by Airbus [9]). But this is out of the scope of the paper. On the other hand, the engines are too slow to be used efficiently during the roll-out phase, with a response time of 6 s. So in practice, they are symmetrically set to idle, *i.e.* $N_{1_{L_c}} = N_{1_{R_c}} = N_{1_{IDLE}}$. Note that the longitudinal motion management can be easily extended to the take-off phase: the mean braking pressure $P_{brk_{COM_c}}$ is simply set to zero and the throttle is set to full thrust, *i.e.* $N_{1_{L_c}} = N_{1_{R_c}} = N_{1_{MAX}}$.

Remark 5. The control architecture has been briefly described in this section for the sake of completeness. It could certainly be improved using the latest advances of the control community, but this is out of the scope of this study. Some strong industrial constraints indeed make it mandatory to improve only one component of this architecture at a time, and this paper focuses on control allocation. This explains for example why faults and disturbances management is not detailed, and why only modal and NDI-based approaches are considered for the design of the guidance and control laws.

5 Control Allocation

Mathematically, an allocator solves an underdetermined system of equations, often subject to additional constraints. It is fed by a vector of virtual inputs $v(t) \in \mathbb{R}^k$ (typically a number of forces and moments that equals the number of degrees of freedom to be controlled), and it delivers the true control inputs $u(t) \in \mathbb{R}^m$ to be sent to the actuators, where $m > k$. In the literature, effector models are almost always linear in u . Thus given $v(t)$, the allocation problem reduces to the computation of $u(t)$ such that:

$$Bu(t) = v(t) \quad (26)$$

for all $t \geq 0$, where $B \in \mathbb{R}^{k \times m}$ is the control effectiveness matrix of rank k . Moreover, actuator rate and position constraints are incorporated such that:

$$u_{min}^p \leq u(t) \leq u_{max}^p \quad , \quad \dot{u}_{min}^r \leq \dot{u}(t) \leq \dot{u}_{max}^r \quad (27)$$

where inequalities apply component-wise. The allocator being embedded in a digital system, rate limits are often converted into effective position limits. The applied limits are then the most restrictive of the position or the converted rate limits:

$$\begin{aligned} \underline{u}(t) &= \max \{ u_{min}^p, u(t-T) + Tu_{min}^r \} \\ \bar{u}(t) &= \min \{ u_{max}^p, u(t-T) + Tu_{max}^r \} \end{aligned} \quad (28)$$

where T is the sample time. Therefore, the standard constrained linear control allocation problem is as follows:

$$Bu(t) = v(t) \quad \text{such that} \quad \underline{u}(t) \leq u(t) \leq \bar{u}(t) \quad (29)$$

Problem (29) has an infinite number of solutions when sufficient control power is available, and a secondary objective can be defined such as minimizing control power. On the contrary, no exact solution exists in case of control power deficiency, and the selected one usually minimizes the L_2 norm $\|Bu - v\|$.

5.1 Control Allocation Techniques Review

From an exhaustive control allocation literature review (including but not limited to [11, 10, 29]), a wide set of methods have been identified. But to be considered flight worthy, an allocation algorithm must reliably produce smoothly varying actuator commands, that do not chatter back and forth from one time step to the next. Furthermore, it should always allow the actuators to produce the largest possible virtual control, or minimize the allocation error in some sense in case of control deficiency [30]. Other factors influencing the choice of some methods over others are determinism,

required computing power and certification aspects. Consequently, some techniques have been discarded due to their intrinsic chattering likelihood or their potential certification issues. For instance, methods based on model predictive control require that a certain desired trajectory be known during a future horizon, which is incompatible with the existing generalized control law, since the pilot yaw rate command profile is not known beforehand. Moreover, methods based on linear matrix inequalities require a prohibitive computational time, while those using online training neural networks are not compatible with the deterministic criteria of the certification authorities.

The most appropriate techniques are summarized in this section, based on their applicability to the considered on-ground aircraft control problem. The L_2 norm of a vector and the Laplace variable are represented by $\|\cdot\|$ and s respectively. The time t is omitted unless it is necessary for understanding.

5.1.1 Unconstrained Methods

The constraint $\underline{u} \leq u \leq \bar{u}$ is removed. It means that $Bu = v$ has an infinite number of solutions, among which the optimal one in the sense of a certain criterion is selected. But it is interesting to note that unconstrained methods may respect actuator position limits to some extent through appropriate choices of some weighting matrices. Moreover, in normal operating conditions, the actuators are seldom saturated in position during ground maneuvers, which makes these easily implementable techniques interesting for the considered application.

Weighted pseudo-inverse [11] It consists in solving the following minimum 2-norm problem:

$$\arg \min_{u \in \mathbb{R}^m} \|W_p^{-1/2} u\| \quad \text{s. t.} \quad Bu = v \quad (30)$$

where $W_p \in \mathbb{R}^{m \times m}$ is a weighting matrix (chosen here as diagonal and composed of the squared position limits of the actuators). It must be emphasized that the maximum attainable v is not accessible with such a constant weighting matrix [31]. Moreover, the actuators do not saturate simultaneously. The solution can be calculated analytically as follows:

$$u = W_p B^T (B W_p B^T)^{-1} v \quad (31)$$

Frequency-apportioned control allocation [32] The desired virtual control v is partitioned into low- and high-frequency components using a low-pass filter $L(s)$:

$$\begin{aligned} v_l &= L(s)v \\ v_h &= [I - L(s)]v \end{aligned} \quad (32)$$

A weighted pseudo-inverse is used to allocate both components according to the actuators position and rate limits:

$$\begin{aligned} u_l &= B_p^\dagger v_l = W_p B^T (B W_p B^T)^{-1} v_l \\ u_h &= B_r^\dagger v_h = W_r B^T (B W_r B^T)^{-1} v_h \end{aligned} \quad (33)$$

where W_p and W_r are weighting matrices (chosen here as diagonal and composed of the squared position and rate limits respectively). The control vector is then given by:

$$u = [B_p^\dagger L(s) + B_r^\dagger (I - L(s))]v \quad (34)$$

A key element in this approach is the selection of the low-pass filter time constant. A method is described in [32].

Linear filter [33] The allocation does not only depend on the current control distribution, but also on the allocation at the previous time step. The following problem is solved:

$$\begin{aligned} \arg \min_{u \in \mathbb{R}^m} & \left\| W_p^{-1/2} u \right\|^2 + \left\| W_r^{-1/2} \Delta u \right\|^2 \\ \text{s. t. } & B u = v \end{aligned} \quad (35)$$

where $\Delta u = u(t) - u(t - T)$ and W_p, W_r are chosen as above. The solution is:

$$u(t) = F u(t - T) + G v(t) \quad (36)$$

where:

$$\begin{aligned} F &= (I - GB)W^{-2}W_r^{-1} \\ G &= W^{-1}(BW^{-1})^T((BW^{-1})(BW^{-1})^T)^{-1} \\ W &= (W_p^{-1} + W_r^{-1})^{1/2} \end{aligned} \quad (37)$$

This method provides a "soft" means to respect rate limits at the expense of position limits violation. But for the considered application, there is no added value compared to the weighted pseudo-inverse since rate limits are rarely violated. And as with the latter, the maximum attainable v cannot be reached.

5.1.2 Basic Constrained Methods

Cascaded generalized inverse [34] It is an iterative heuristics based on the pseudo-inverse method. Position saturated controls are removed from subsequent pseudo-inverse solutions until either all control effectors saturate or a solution is found that does not violate actuator constraints.

Daisy chaining [11] A hierarchy is established between the control effectors, which are separated into different groups. The control inputs are computed assuming that only the first group of effectors is used. As soon as one of them exceeds the position limits, the overflow is sent to the second group and so on. For the considered application, the first group consists of the classical actuators, *i.e.* the NWS system and the rudder, and the second one consists of differential braking. Allocation within the first group is done using the pseudo-inverse method of Section 5.1.1. It could be done with any other technique, but the pseudo-inverse method is used here for its low computational power requirement. Note that differential braking is not minimized with this strategy, since it is used as soon as one actuator of the first group saturates. A way to address this issue could be to send the overflow of \dot{r}_{act_c} to the other actuator of the first group before using the second group.

5.1.3 Solver-based Methods

Weighted least squares (LS) It consists in solving the following weighted least squares problem:

$$\arg \min_{\underline{u} \leq u \leq \bar{u}} \left\| W_p^{-1/2} u \right\|^2 + \gamma \|Bu - v\|^2 \quad (38)$$

where $W_p \in \mathbb{R}^{m \times m}$ is a weighting matrix chosen as in (30) and γ is set to a large value, indicating the priority of error minimization over that of control minimization. This can be done using the MATLAB *quadprog* solver, an active set solver [33], an interior point solver [35] or a fixed-point iteration algorithm [36].

Sequential least squares [33] It consists in solving the following sequential least squares problem using an active set solver, where W_p is chosen as above:

$$\arg \min_{u \in \Omega} \left\| W_p^{-1/2} u \right\| \quad \text{where } \Omega = \arg \min_{\underline{u} \leq u \leq \bar{u}} \|Bu - v\| \quad (39)$$

Minimal least squares [33] A minimal least squares problem (see [37]) formulated in the same way as (39) is solved using a two-stage active set method. W_p must be diagonal, which is the case here. However, this implementation does not handle the case of coplanar controls.

Direct allocation The following direct allocation problem is considered in [31]:

$$\max_{\rho \leq 1} \rho \quad \text{subject to} \quad \begin{cases} Bu = \rho v \\ u_{min}^p \leq u \leq u_{max}^p \end{cases} \quad (40)$$

which consists of finding the best approximation of v satisfying the control constraints and being colinear to v . It is solved either geometrically in [31] or reformulated as a linear programming problem and solved using the simplex method in [38]. The set of admissible control inputs must include 0, which leads to considering the bounds u_{min}^p and u_{max}^p instead of \underline{u} and \bar{u} as in most other methods. Indeed, unlike \underline{u} and \bar{u} , u_{min}^p and u_{max}^p generally satisfy $u_{min}^p < 0 < u_{max}^p$ in practice.

Dynamic allocation [33] It extends regular quadratic programming control allocation by also penalizing the actuator rates and is formulated as follows:

$$\arg \min_{u \in \Omega} \left\| W_p^{-1/2} u \right\|^2 + \left\| W_r^{-1/2} \Delta u \right\|^2 \quad (41)$$

where $\Omega = \arg \min_{\underline{u} \leq u \leq \bar{u}} \|Bu - v\|$

W_p and W_r are chosen as above, and Δu is defined as in (35). Problem (41) is solved using an active set solver in [33].

Remark 6. *Robust control allocation techniques taking into account uncertainties and actuator faults are proposed in [39, 40]. They are mainly variations of the aforementioned solver-based techniques. They are not considered in this study, which does not focus primarily on uncertainties and faults.*

5.1.4 Iterative Methods

Nullspace-based pseudo-inverse [41] The pseudo-inverse is used as a primal solution, which is then modified using the nullspace of the control effectiveness matrix. This method handles non-symmetric actuator limits, hence rate limits (see (28)). Moreover, an appropriate solution is given even in the presence of singularity and is guaranteed with a predefined computational burden, which is a non-negligible advantage over linear and quadratic optimization methods.

Fixed point methods [42] The constrained control allocation problem is formulated into an equivalent fixed point problem. Two algorithms are proposed:

- a sequential method, similar to the algorithms given in [36], but which adopts a different approach for satisfying the convergence criteria,
- a Newton method, where the consideration of the saturation function leads to a nonsmooth zero finding problem, and which guarantees superlinear convergence.

Dynamical pseudo-inverse [43] Under the assumption that at least one solution to the allocation problem under saturation exists, two algorithms are proposed which provide a suitable symmetric positive weighting matrix W leading to that solution:

- a linear control allocation algorithm which computes W for the following allocation law linear in W :

$$u = [I + (I - B^T(BB^T)^{-1}B)W]B^T(BB^T)^{-1}v \quad (42)$$

- a nonlinear control allocation algorithm which computes W for the following allocation law nonlinear in W :

$$u = WB^T(BWB^T)^{-1}v \quad (43)$$

W is adjusted only during saturation until values of u are found which satisfy the constraint $\underline{u} \leq u \leq \bar{u}$. However, such an approach does not generally minimize the total control effort, which is often an important requirement.

Karush-Kuhn-Tucker (KKT)-based algorithm [44] It consists of solving several systems of equations to find all the local optimal solutions, and consequently the global one through a simple comparison between all realistic local minima. This algorithm is independent on the selection of initial conditions, since the considered nonlinear optimization problem is converted into classical eigenvalue problems.

5.1.5 Update Law-based Methods

Dynamic control allocator [45] It aims at injecting an arbitrary signal in certain input directions, which does not modify the state response or the steady-state output response. This arbitrary signal is the output of a suitable number of integrators, whose states are adjusted online based on certain gains intuitively chosen to promote or penalize the different actuators based on their rate or magnitude saturation levels. When implemented on a digital system, there is a strong limit in the dynamic allocation speed to ensure stability. Therefore, the initial allocation should not be too far from the optimal solution, which is already an allocation problem in itself.

5.2 Benchmark

The allocation techniques identified in Section 5.1 are now applied to the on-ground control problem stated in Section 2. As further detailed in Section 5.2.1, the whole lateral ground control architecture of Figure 6 is not considered for the moment. The objective is indeed to focus on the allocation algorithms to determine whether they are able to compute quickly and

reliably some admissible actuator commands, which produce a yaw acceleration \dot{r}_{act} (almost) equal to the reference value \dot{r}_{act_c} issued by the yaw rate controller. The considered benchmark is shown in Figure 7 and is composed of four blocks described in Sections 5.2.1 to 5.2.4. A thorough comparison of all allocation techniques is then performed in Sections 5.2.5 and 5.2.6 on a realistic worst-case scenario.

5.2.1 Scenario

The yaw rate controller described in Section 4 normally computes a virtual input $v = \dot{r}_{act_c}$ corresponding to the commanded yaw acceleration to be produced by the actuators. For this benchmark, a \dot{r}_{act_c} profile recorded during a real landing with difficult operating conditions is used instead. This is indeed a convenient way to push the allocation module to the limits for a better evaluation, and explains why an open-loop benchmark is considered in this section. More precisely, the commanded yaw acceleration \dot{r}_{act_c} issued by the **Scenario block** corresponds to a landing with 30 kt of crosswind turbulence, as well as 20 kt of lateral gust occurring when the aircraft speed is 100, 60 and 40 kt.

5.2.2 Computation of the Yaw Acceleration

Based on the on-ground aircraft model developed in Section 3, the **Yaw block** computes the part \dot{r}_{act} produced by the actuators of the total yaw acceleration \dot{r} :

$$\dot{r}_{act} = \dot{r}_{\delta r} + \dot{r}_{NW} + \dot{r}_{brk_{MGL}} + \dot{r}_{brk_{MGR}} \quad (44)$$

It depends on various parameters (ground speed, lever arms with respect to the centre of gravity, runway state...). The rudder and the nose-wheel contributions are given by:

$$\dot{r}_{\delta r} = \frac{q_d S c C n_{\delta r} \delta r}{I_{zz}} \quad (45)$$

$$\dot{r}_{NW} = \frac{D x_{NW}}{I_{zz}} \bar{F}_{sy_{NW}} \quad (46)$$

where $\bar{F}_{sy_{NW}}$ is obtained from (10) as:

$$\bar{F}_{sy_{NW}} = \bar{\mu} \mu_{MAX} F_{z_{NW}} \tanh\left(\frac{K_{y_{NW}} \theta_{NW}}{\bar{\mu} \mu_{MAX}}\right) \quad (47)$$

Remark 7. *The yaw acceleration produced by the nose-wheel rolling resistance is negligible compared to that produced by the lateral slip force and is hence neglected in (46).*

The yaw accelerations produced by the braking systems are:

$$\begin{aligned}\dot{r}_{brk_{MGL}} &= -\frac{Dy_{MG}}{I_{zz}}F_{sx_{MGL}} \\ \dot{r}_{brk_{MGR}} &= \frac{Dy_{MG}}{I_{zz}}F_{sx_{MGR}}\end{aligned}\quad (48)$$

Finally, the engine throttles are both set to idle and therefore do not appear here.

5.2.3 Control Allocator

As highlighted in Section 5, the **Control Allocation block** receives the virtual control input $v = \dot{r}_{act_c}$ and computes the real control inputs u to be sent to the actuators. In order to minimize the effect of differential braking on the longitudinal motion, ganging of the left and right braking systems is considered: $\delta P_{brk_c} = P_{brk_{MGR_c}} - P_{brk_{MGL_c}}$ is computed, and $P_{brk_{MGR_c}} = 0.5\delta P_{brk_c}$ and $P_{brk_{MGL_c}} = -0.5\delta P_{brk_c}$ are then applied in the **Actuators block**, which directly implements the models of Section 3.3. Thus, the number of outputs of the control allocator reduces to $m = 3$ and the matrices of (29) are given by:

$$\begin{aligned}u &= [\theta_{NW_c} \ \delta r_c \ \delta P_{brk_c}]^T \\ v &= \dot{r}_{act_c} \\ B &= \left[\begin{array}{ccc} \frac{\partial \dot{r}_{act}}{\partial \theta_{NW}} & \frac{\partial \dot{r}_{act}}{\partial \delta r} & \frac{1}{2} \left(\frac{\partial \dot{r}_{act}}{\partial P_{brk_{MGR}}} - \frac{\partial \dot{r}_{act}}{\partial P_{brk_{MGL}}} \right) \end{array} \right] \\ &= \left[\begin{array}{ccc} \frac{Dx_{NW}K_{y_{NW}}F_{z_{NW}}}{I_{zz}} & \frac{\rho V_a^2 Sc Cn_{\delta r}}{2I_{zz}} & \frac{Dy_{MG}N_{t_{MG}}G_{brk}}{I_{zz}R_e} \end{array} \right]\end{aligned}$$

The saturations and asymptotic limits of the ground reaction forces (47) and (48) are dropped in the computation of the control effectiveness matrix B . They are taken into account indirectly by more restrictive actuator position limits:

$$u_{max}^p = -u_{min}^p = [L_{p_{NW_{CA}}} \ L_{p_{\delta r_{CA}}} \ L_{p_{brk_{CA}}}]^T \quad (49)$$

5.2.4 Key Performance Indicators

To be deemed flight worthy, a control allocator should converge in a minimum time (less than the sample time), and in a minimum number of iterations. Most if not all virtual controls should be attained within the capacity of the actuators, therefore minimizing an equivalent yaw acceleration error. Lastly, actuators use should be minimized as far as possible. In this context, the following indicators, taken both from [41] and from Airbus expertise in world civil aviation, are chosen to assess the performance of the control allocation techniques.

- mean and maximum number of iterations,
- mean convergence time over all sampling periods and over the worst 10%,
- integral of squared error: $\int (\dot{r}_{act_c} - \dot{r}_{act})^2 dt$,
- normalized consumption: $\int (|u| \oslash u_{max}^p) dt$, where \oslash denotes the Hadamard (*i.e.* element-wise) division.

Remark 8. The first four indicators are given per sampling period (40 ms for the considered benchmark). The last two are computed numerically over several thousand sampling periods.

5.2.5 Benchmark Setup

The allocation methods presented in Section 5.1 are now evaluated on the benchmark. More precisely, each of them is successively implemented in the **Control Allocation block**, all the other blocks remaining unchanged, and the scenario described in Section 5.2.1 is executed. The MATLAB implementations of all solver-based algorithms, except the *quadprog* solver which is part of the Optimization Toolbox, are available online in the *QCAT* Toolbox (<http://research.harkegard.se/qcat>). They have only been slightly adapted for the benchmark. All the other algorithms have been coded from scratch.

The performance indicators described in Section 5.2.4 are shown in Table 3. N/A means that the considered indicator is not applicable, *i.e.* the corresponding method is not iterative. The convergence time should be interpreted with caution, since it was obtained using the MATLAB *tic/toc* functions, which depend on the CPU consumption of background applications. Nevertheless, it provides a rough estimate of the computational burden and allows relative comparison between the methods.

5.2.6 Results Analysis

The following conclusions are drawn from the considered benchmark, and they may therefore not be generalizable.

The *convergence time* is within the same order of magnitude for all methods except direct allocation, which is almost 10 times slower. A similar comparison was reported in [46]. For the weighted LS problem (38), the active set solver outperforms the MATLAB *quadprog* solver. Indeed, it uses the solution from the previous sample as an initial guess to hot start the algorithm, which yields faster convergence.

Most methods make use of a constant user-defined weighting matrix W_p to minimize the weighted control vector $W_p^{-1/2}u$ and to avoid as far as possible to reach actuator saturations. The frequency-apportioned, the linear

Method	Mean # of iterations	Max # of iterations	Mean conv. time [ms]	Mean worst 10% conv. time [ms]	Integral of squared error [$\times 10^{-3}$ deg/s ²]	Normalized consumption
Weighted pseudo-inverse [11]	N/A	N/A	2.77	3.31	1.0389	81.3319
Frequency-apportioned control allocation [32]	N/A	N/A	2.82	3.36	1.2341	84.9120
Linear filter [33]	N/A	N/A	3.27	5.10	1.6442	88.5882
Cascaded generalized inverse [34]	1.0	2	2.84	3.41	1.0389	81.3322
Daisy chaining [11]	N/A	N/A	2.39	5.78	1.3013	75.3898
Weighted LS - <i>quadprog</i> solver	3.4	5	7.75	10.36	1.0562	81.6594
Weighted LS - active set solver [33]	1.0	2	2.92	3.51	1.0389	81.3228
Weighted LS - interior point solver [35]	1.7	2	2.97	3.55	1.7884	108.7635
Weighted LS - fixed-point algorithm [36]	100	100	2.97	3.55	1.8588	110.0601
Sequential LS [33]	2.0	3	3.08	3.68	1.0389	81.3322
Minimal LS [33]	2.0	3	3.00	3.63	1.0389	81.3322
Direct allocation [38]	1.3	2	20.42	26.33	1.6106	107.4062
Dynamic allocation [33]	1.0	2	3.10	3.73	1.0430	81.3329
Nullspace-based pseudo-inverse [41]	1.0	2	3.24	4.01	1.0389	81.3321
Fixed point - sequential method [42]	28.1	47	2.97	3.60	1.0390	81.3316
Fixed point - Newton method [42]	2.0	4	3.04	3.63	1.0389	81.3315
Linear dynamical pseudo-inverse [43]	N/A	N/A	2.84	3.38	1.5504	104.1167
Nonlinear dynamical pseudo-inverse [43]	N/A	N/A	2.86	3.40	1.5853	105.7331
KKT-based algorithm [44]	27	27	3.71	5.81	1.0389	81.3321
Dynamic control allocator [45]	N/A	N/A	3.08	3.80	1.0359	81.8253

Table 3: Benchmark synthetic results

filter and the dynamic allocation methods also use an additional weighting matrix W_r , which penalizes actuator rates. However, there is no added value for the considered benchmark, since rate limits are rarely violated.

The fixed-point iteration algorithm [36] converges to the optimal solution as the *number of iterations* goes to infinity. Here, the number of iterations is limited to 100 and therefore, this method presents the highest allocation error and normalized actuators consumption. The number of iterations of the KKT-based algorithm is equal to 3^m , which corresponds to all the combinations of the 3 possible states of each of the m actuators (lower or upper saturated, or not saturated). In contrast, the number of iterations remains quite low for all other iterative techniques. But interestingly, several non-iterative approaches are as good or even better in terms of error and consumption. They are preferred here, since they make the certification process easier. Among them, the weighted pseudo-inverse and the daisy chaining presented in [11], the linear filter from [33] and the dynamic allocator described in [45] have the added advantage of being easily implemented. *They can thus be considered as the most relevant approaches in the present context.*

But they suffer from a certain number of drawbacks. First, the maximum attainable \dot{r}_{act_c} is not accessible with a constant weighting matrix W_p [31]. Moreover, the classical actuators (NWS system and rudder) do not saturate simultaneously when W_p is composed of the squared position limits of the actuators. Then, the weighted pseudo-inverse and the linear filter techniques do not consider actuator saturations at all, which could lead to disappointing results in case of extreme scenarios, and the dynamic allocator requires to find an initial solution which is close to the optimal one when implemented on a digital system. Finally, no method allows to minimize brakes use,

except daisy chaining to a certain extent by placing the braking systems in the secondary group of actuators. But even then, the classical actuators do not reach saturation simultaneously and the brakes are activated before they are all saturated.

Therefore, *a new allocation algorithm should be developed* to comply with the control objectives stated in Section 2. In view of the above, the idea is to build upon the weighted pseudo-inverse, which despite its disadvantages is very easy to implement and use. On the other hand, comparisons will be made with the daisy chaining, which among the existing methods is the one that is best suited to the problem under consideration.

6 Proposed Control Allocation Technique

The Dynamic Weighting Control Allocator (DWCA), summarized in Algorithm 1, is a pseudo-dynamical control allocation technique, which intelligently manages the trade-off between minimizing actuators use and attaining the maximum virtual control in the 1-dimension case, *i.e.* $v \in \mathbb{R}$. It meets the specifications of Section 2 and respects various practical requirements, such as limited computational power and implementation constraints. It also allows the consideration of actuator dynamics.

Algorithm 1 Proposed control allocation method

Require: B , v , u_{min}^p and u_{max}^p
 Compute $u_{lim_i}^p$ as in (54)
if $B_U = 0$ **then**
 Compute B_S as in (53)
 if $B_S = 0$ **then**
 Compute w_i as in (55)
 else
 Compute w_i as in (56)
 end if
else
 Compute w_i as in (57)
end if
 Filter \bar{w}_i as in (58)
 Compute u_i as in (52)
return u

Remark 9. *To make the equations simpler, it is assumed in this section that $u_{min}^p < 0 < u_{max}^p$, which is almost always the case in practice. But Algorithm 1 can be easily extended to any values of u_{min}^p and u_{max}^p .*

The DWCA requires that the m actuators be grouped as "primary" or "secondary". In the *nominal mode*, actuators from the primary group are

first used up to their maximum capability. They are used according to their relative efficiency and reach saturation almost simultaneously, which is not possible with daisy chaining for example. Only then are the actuators from the secondary group used. The DWCA also presents an *unrestricted mode* activated by the boolean B_U , which considers all available actuators as primary. This mode may be triggered for instance according to the lateral deviation from the runway centerline, the orientation of the aircraft and the runway state (*e.g.* when $\bar{\mu}$ is below a given threshold).

The DWCA is based on the weighted pseudo-inverse approach mentioned in Section 5.1.1 and requires to solve:

$$\arg \min_{u \in \mathbb{R}^m} \frac{1}{2} u^T W^{-1} u \quad \text{subject to} \quad Bu = v \quad (50)$$

where $W \in \mathbb{R}^{m \times m} = \text{diag}(\bar{w}_1, \dots, \bar{w}_m)$ is a weighting matrix, $B = [b_1 \dots b_m] \in \mathbb{R}^{1 \times m}$ and $v \in \mathbb{R}$. The general solution is:

$$u = WB^T(BWB^T)^{-1}v \quad (51)$$

The commanded deflection for the i^{th} actuator is then given by:

$$u_i = \text{sat} \left[u_{\min_i}^p, u_{\max_i}^p \right] \left(\frac{b_i \bar{w}_i}{\sum_{j=1}^m b_j^2 \bar{w}_j} v \right) \quad (52)$$

where b_i is the efficiency of the i^{th} actuator, and the saturation operator is defined such that $\text{sat}_{[F_1, F_2]}(x) = x$ if $F_1 \leq x \leq F_2$, $\text{sat}_{[F_1, F_2]}(x) = F_1$ if $x < F_1$ and $\text{sat}_{[F_1, F_2]}(x) = F_2$ if $x > F_2$. *The originality of the proposed approach lies in the choice of the \bar{w}_i , which depends on the values taken by the booleans B_U and B_S .*

Consider the first n and the last l actuators, such that $n+l = m$, as part of the primary and secondary groups respectively. While the *unrestricted mode* is not activated ($B_U = 0$), the use of the secondary group is triggered by B_S when the virtual command v cannot be realized using exclusively the primary group:

$$B_S = \begin{cases} 1 & \text{if } |v| > \eta_{DWCA} v_n \\ 0 & \text{otherwise} \end{cases} \quad (53)$$

where $v_n = \sum_{j=1}^n |b_j| u_{\lim_j}^p$ is the absolute value of the maximum virtual control in the direction of v that can be generated by the primary actuators. The efficiency η_{DWCA} of the control allocator is typically set between 0.9 and 1, so that the secondary actuators begin to be used slightly before all actuators from the primary group reach saturation, allowing some kind of “phase advance”. The effective limit $u_{\lim_i}^p$ of each actuator is given by:

$$u_{lim_i}^p = \begin{cases} u_{max_i}^p & \text{if } b_i v \geq 0 \\ |u_{min_i}^p| & \text{otherwise} \end{cases} \quad (54)$$

In the *nominal mode*, when the use of the secondary group is not required ($B_S = 0$), the following weighting parameters are defined:

$$w_{i \in \{1, \dots, n\}}(t) = \left(u_{lim_i}^p\right)^2 + \left(\frac{1}{|b_i|} - u_{lim_i}^p\right) |u_i(t - T)| \quad (55a)$$

$$w_{i \in \{n+1, \dots, m\}}(t) = 0 \quad (55b)$$

The weights of the secondary actuators are set to zero in (55b). Those of the primary actuators are defined as the sum of two terms in (55a): the control power minimization term $\left(u_{lim_i}^p\right)^2$ and the maximum virtual control reaching term $\left(\frac{1}{|b_i|} - u_{lim_i}^p\right)$. The trade-off between these two antagonist terms depends on the commanded actuator deflection at the previous time step $u_i(t - T)$. When $|u_i(t - T)|$ is small, $w_i \approx \left(u_{lim_i}^p\right)^2$ and control power is minimized. But when $|u_i(t - T)|$ is close to $u_{lim_i}^p$, $w_i \approx \frac{u_{lim_i}^p}{|b_i|}$. In this case, if the filtering effect of (58) is ignored, *i.e.* $\bar{w}_i = w_i$, (52) becomes $u_i \approx \text{sat}\left[u_{min_i}^p, u_{max_i}^p\right] \left(\frac{|v|}{v_n} \text{sign}(b_i v) u_{lim_i}^p\right)$. Noting that $\text{sign}(b_i v) u_{lim_i}^p$ is equal to $u_{max_i}^p$ if $b_i v \geq 0$ and $u_{min_i}^p$ if $b_i v < 0$, this shows that the ratio $|v|/v_n$ between the actual position and the position limit is the same for all primary actuators. Therefore, the latter reach saturation at the same time when the virtual control v reaches v_n .

When the use of the secondary actuators is deemed necessary ($B_S = 1$), the following weighting parameters are used:

$$w_{i \in \{1, \dots, n\}}(t) = \frac{u_{lim_i}^p}{|b_i|} \quad (56a)$$

$$w_{i \in \{n+1, \dots, m\}}(t) = \frac{u_{lim_i}^p}{|b_i|} \min\left(1, \frac{|v| - \eta_{DWCA} v_n}{v_l}\right) \quad (56b)$$

where $v_l = \sum_{j=n+1}^m |b_j| u_{lim_j}^p$ is the absolute value of the maximum virtual control in the direction of v that can be generated by the secondary actuators. The primary actuators are set to their maximum deflections in (56a), while the secondary ones are set to the minimum required deflections in (56b), with bounds equal to their position limits.

In the *unrestricted mode* ($B_U = 1$), the weighting parameter of each actuator is given by:

$$w_{i \in \{1, \dots, m\}}(t) = \left(u_{lim_i}^p\right)^2 + \left(\frac{1}{|b_i|} - u_{lim_i}^p\right) |u_i(t - T)| \quad (57)$$

In this case, all actuators are used the same way to manage the trade-off between minimizing control power and attaining the maximum virtual control.

Before computing the commanded deflections (52), the dynamics of each actuator is catered for by filtering the corresponding weighting parameter w_i from (55)-(57) through a first order filter of time constant τ_i equal to that of the i^{th} actuator:

$$\bar{w}_i(t) = \frac{1}{1 + \tau_i s} w_i(t) \quad (58)$$

7 Results and Analysis

The effectiveness of the DWCA is assessed through open- and closed-loop simulations. The method is also thoroughly compared to the most relevant existing technique identified in Section 5.2.6, namely daisy chaining. In this study, the primary group is composed of the NWS system and the rudder, while differential braking forms the secondary group.

7.1 Open-loop Evaluation

The allocation techniques identified in Section 5.1 and the DWCA are first compared on 3 scenarios corresponding to realistic \dot{r}_{act_c} profiles which:

1. can be realized using the conventional actuators only,
2. can be realized using all actuators,
3. cannot be realized with all actuators at their limits.

The used indicators, in decreasing order of importance, are:

- *percentage of unrealized virtual control*: percentage of time during which $|Bu - v| > \epsilon$ (10^{-5} here).
- *percentage of differential braking*: ratio δP of the normalized consumption of differential braking to the sum of the normalized consumption of each actuator,
- *integral of squared error*: $\int (\dot{r}_{act_c} - \dot{r}_{act})^2 dt$,
- *normalized consumption*: $\int (|u| \oslash u_{max}^p) dt$.

Virtual control realization and differential braking minimization being the main objectives, Table 4 confirms that daisy chaining is the most efficient existing technique, but is outperformed by the DWCA. Indeed, it uses almost twice as much differential braking, since it starts using brakes although both conventional actuators are not saturated. Brakes being the fastest actuators, this also explains why it has a slightly lower error. *Therefore, the best open-loop results are obtained with the DWCA.*

Method	Unrealized control [%]	Ratio δP [%]	Integral of squared error [$\times 10^{-3}$ deg/s ³]	Normalized consumption
Weighted pseudo-inverse	7	19	3.1	42.4
Linear filter	7	19	3.1	42.4
Daisy chaining	8	9	1.8	41.1
Dynamic control allocator	37	11	11.5	126.4
DWCA (Section 6)	7	5	2.5	42.2

Table 4: Open-loop synthetic results

7.2 Closed-loop Evaluation - Simulink

The DWCA is now compared to daisy chaining in closed-loop using the control architecture described in Section 4. In both cases, the aircraft is initialized at 120 kt on a dry runway with a lateral deviation of 8 m, and the maneuver is stopped when the ground speed reaches 20 kt. A constant tail wind of 15 kt and a lateral turbulence reaching a peak of 43 kt are used, as illustrated in Figure 8. The longitudinal distance X_G is arbitrarily set to zero at the beginning of the simulations. The unrestricted mode is not activated, so as to show the efficiency of the DWCA in reducing the use of the brakes. It can be seen in Figure 9 that both control allocators maintain the aircraft on the runway with a negligible trajectory difference. Moreover, the lateral load factor N_y represented in Figure 10 remains under $0.1g$, which is an acceptable level of comfort given the fairly strong crosswind. In contrast, when the unrestricted mode is activated, the aircraft reaches the runway centerline faster with the DWCA than with daisy chaining with a comparable use of the brakes (plots are omitted here due to space constraints).

The commanded and the realized virtual controls for the DWCA are shown in Figure 11. The realized one lags behind the commanded one due to the actuator dynamics. It can also be noticed that the command cannot be realized at 25s and 36s since all 3 actuators are saturated (30 deg for the rudder, 30 bars for the brakes and 6 deg for the nose-wheel, see Figure 12b). With daisy chaining, a similar trend is observed where the virtual control cannot be realized at the same moments as with the DWCA. It is very important to note that daisy chaining uses more differential braking, especially when the NWS has not reached saturation, as can be seen by comparing Figures 12a and 12b. Globally, daisy chaining does not minimize the use of the brakes, which results in 14% more differential braking than with the DWCA. *Thus, the DWCA is more relevant on the considered scenario.*

7.3 Closed-loop Evaluation - High-fidelity Airbus Simulator

The DWCA is now implemented in the high-fidelity long-range Airbus simulator with the control architecture of Section 4. The lateral deviation being strongly dependent on the lateral wind and the runway state, the latter are varied significantly in the following validation tests.

7.3.1 Comparison with an Airbus reference control allocator

The DWCA is first compared to a reference Airbus control allocator, which is not detailed here since it contains proprietary data. Two classical validation tests are performed:

T1: gaussian crosswind on dry and wet runways,

T2: crosswind of 30 kt with gust on dry and wet runways.

during which the allocators and the control laws always assume that the runway is dry. For each test, the same 2000 simulations are performed for both allocators. They allow to cover as much as possible the entire operational domain:

- mass varying between light and heavy aircraft,
- center of gravity location varying between max aft and max forward values,
- different slats and flaps configuration,
- varying lateral deviation at touchdown,
- different deceleration rates.

Results are shown in Table 5, where *Norm. mean 50 w.c.* corresponds to the normalized mean lateral deviation for the 50 worst cases (its value is always equal to 1 for the reference allocator). The test T1 is the less demanding one and the reference allocation already performs well, which explains why the lateral deviation cannot be improved by the DWCA. Nevertheless, the normalized consumption is much lower with the latter algorithm, with a reduction of 27%. By contrast, the improvement is noticeable for the test T2. The mean lateral deviation is reduced by almost 15% and the lateral excursion is less dispersed with the DWCA. Moreover, the lateral deviation is decreased by 27% for the 50 worst cases, and the actuators use by 34%, positively influencing actuator sizing and lifespan. *Results are thus strongly in favor of the DWCA.*

Test	Reference allocator	DWCA	
T1	Lateral deviation		
	Mean value [m]	2.20	2.25
	Standard deviation [m]	1.03	1.05
	Norm. mean 50 w.c.	1	0.99
	Actuators consumption (see Section 7.1)		
	Normalized	1	0.73
T2	Lateral deviation		
	Mean value [m]	6.23	5.27
	Standard deviation [m]	3.05	2.16
	Norm. mean 50 w.c.	1	0.73
	Actuators consumption (see Section 7.1)		
	Normalized	1	0.66

Table 5: Summary of T1-2 results

7.3.2 Evaluation on contaminated runways and robustness

The DWCA is now evaluated on contaminated runways with 2000 simulations for each runway state and the same varying conditions as in Section 7.3.1. The following test is performed:

T3: crosswind with gust of consistent magnitude with the runway state on flooded, snowy, slushed and icy runways.

during which it is assumed that the control tower communicates the real runway state to the allocator and the control laws. Then, a robustness analysis is performed whereby the allocator and the control laws assume that the runway is dry while it is wet and vice-versa. This case can easily be encountered when the runway state evolves after the information is sent by the control tower. This leads to the following tests (2000 simulations each):

T4: crosswind of 30 kt with gust on dry runway while the control laws assumes a wet runway,

T5: crosswind of 30 kt with gust on wet runway while the control laws assumes a dry runway.

As can be seen in Table 6, the results of T3 are comparable to the results obtained with the DWCA in T2 and more favorable than those obtained with the reference allocator. This shows that the DWCA performs well whatever the runway state. T4 and T5 then show that a wrong runway state information has a very moderate effect on the DWCA performance, since the mean lateral deviation is only 2.2% larger than when the real runway state is known. A justification for this is that a confusion between

Test		DWCA	% variation <i>w.r.t.</i> real runway state
T3	Mean value [m]	5.06	N/A
	Standard deviation [m]	2.45	N/A
T4	Mean value [m]	5.02	-0.9%
	Standard deviation [m]	2.11	+0.5%
	Norm. mean 50 w.c.	1	1
T5	Mean value [m]	5.77	+2.2%
	Standard deviation [m]	2.59	+1.4%
	Norm. mean 50 w.c.	1	1.02

Table 6: Lateral deviation for T3-5

dry and wet induces a maximum error of 10% on the reduced cornering gains K_{y_k} according to (11), which is covered by the robustness margin of the control laws. Results would probably be worst in case of a larger runway state estimation error. But this is unlikely to happen, since the information communicated by the control tower is only slightly erroneous in practice.

8 Conclusion

An accurate on-ground aircraft model of tractable complexity is first proposed in this paper to address various control issues such as runway centerline tracking. It bridges the gap between high-fidelity but complicated models intended for simulation and over-simplified ones. Precise descriptions of the tire-ground interactions, of the dependences to the vertical load and the runway state, and of all available actuators, are notably provided. A complete set of numerical values representative of a commercial aircraft is included, as well as design objectives, so as to provide the control community with a challenging benchmark. A thorough comparison of the most relevant existing control allocation techniques is then presented on a realistic worst-case landing scenario. Based on these results, a novel and easily implementable allocation technique is finally introduced to solve the allocation problem raised by the yaw control of an on-ground aircraft. It ensures the safety of the aircraft while minimizing the use of the brakes, which is a strong industrial requirement. It also manages the compromise between virtual control realization and control power minimization. The conventional actuators come to saturation almost simultaneously, which increases the fault recovery capability, and actuator dynamics are taken into account. Finally, it meets the aircraft manufacturer and the certification authorities requirements. The open- and closed-loop simulations performed on the proposed on-ground aircraft model show the effectiveness of the method in

comparison with several other allocation strategies, especially daisy chaining. Moreover, statistical results on a high-fidelity Airbus simulator reveal that the lateral deviation and the actuators use are significantly reduced in difficult situations such as strong crosswind compared to an Airbus reference control allocator. It is worth pointing out that the scope of application is broader than that presented in this paper, and the proposed algorithm is applicable to any axis of the general vehicle control problem (aerial, space, automotive, submarine...). Future work will notably be dedicated to the better estimation of the ground effectors efficiency with the development of a runway state estimator. Finally, flight tests on a real aircraft are scheduled in the short term.

Acknowledgment

This research is supported by Airbus Operations S.A.S., the National Association of Research and Technology (ANRT) and the French Ministry of Higher Education, Research and Innovation under the *CIFRE* contract 2016/1058. The authors thank Jean Muller for his kind help with the high-fidelity simulations.

Conflict of interest

The authors declare that there is no conflict of interest.

References

- [1] P. Traverse, I. Lacaze, J. Souyris, Airbus fly-by-wire: A total approach to dependability, in: Proceedings of the 18th IFIP World Computer Congress, Toulouse, France, 2004, pp. 191 – 212.
- [2] Eurocontrol, European action plan for the prevention of runway excursions, Tech. rep., Eurocontrol (2013).
- [3] G. W. H. van Es, A study of runway excursions from a european perspective, Tech. Rep. NLR-CR-2010-259, Eurocontrol (2010).
- [4] C. Roos, J.-M. Biannic, S. Tarbouriech, C. Prieur, M. Jeanneau, On-ground aircraft control design using a parameter-varying anti-windup approach, *Aerospace Science and Technology* 14 (7) (2010) 459 – 471.
- [5] D. Lemay, Y. Chamailard, M. Basset, J. P. Garcia, Gain-scheduled yaw control for aircraft ground taxiing, in: Proceedings of the 18th IFAC World Congress, Milan, Italy, 2011, pp. 12970 – 12975.

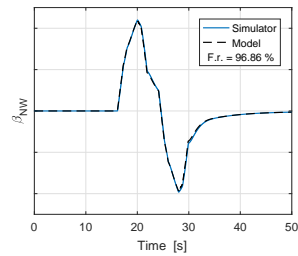
- [6] G. Looye, Chapter 8: Rapid prototyping using inversion-based control and object-oriented modelling, in: D. Bates, M. Hagström (Eds.), *Non-linear Analysis and Synthesis Techniques for Aircraft Control*, Lecture Notes in Control and Information Sciences, vol. 365, Springer-Verlag Berlin Heidelberg, 2007, pp. 147 – 173.
- [7] F. Villaumé, *Contribution à la commande des systèmes complexes : Application à l'automatisation du pilotage au sol des avions de transport*, Ph.D. thesis, Université Toulouse III - Paul Sabatier, Toulouse, France (2002).
- [8] J. Duprez, F. Mora-Camino, F. Villaumé, Control of the aircraft-on-ground lateral motion during low speed roll and manoeuvres, in: *Proceedings of the IEEE Aerospace Conference*, Big Sky, USA, 2004, pp. 2656 – 2666.
- [9] F. Villaumé, T. Lagaille, Runway overrun prevention system (ROPS), Tech. Rep. FAST#55, Airbus (2015).
- [10] T. A. Johansen, T. I. Fossen, Control allocation – A survey, *Automatica* 49 (5) (2013) 1087 – 1103.
- [11] M. W. Oppenheimer, D. B. Doman, M. A. Bolender, Chapter 8: Control allocation, in: W. S. Levine (Ed.), *The Control Handbook*, Control System Applications (Second Edition), CRC Press, 2010, pp. 1 – 24.
- [12] E. Sadien, C. Roos, A. Birouche, M. Carton, C. Grimault, L. E. Romana, M. Basset, A detailed comparison of control allocation techniques on a realistic on-ground aircraft benchmark, in: *Proceedings of the American Control Conference*, Philadelphia, USA, 2019, pp. 2891–2896.
- [13] K. Brüggemann, B. Cheray, L. E. Romana, Brake wear reduction apparatus, JUSTIA Patents, patent number 20180079402. <https://patents.justia.com/patent/20180079402> (2017).
- [14] C. Bihua, J. Zongxia, S. S. Ge, Aircraft-on-ground path following control by dynamical adaptive backstepping, *Chinese Journal of Aeronautics* 26 (3) (2013) 668 – 675.
- [15] J.-M. Biannic, A. Marcos, M. Jeanneau, C. Roos, Nonlinear simplified LFT modelling of an aircraft on ground, in: *Proceedings of the IEEE International Conference on Control Applications*, Munich, Germany, 2006, pp. 2213 – 2218.
- [16] M. C. Turbuk, P. Paglione, Aircraft ground dynamics modeling, in: *Proceedings of the VI National Congress of Mechanical Engineering*, Campina Grande, Paraiba, Brazil, 2010, pp. 1 – 9.

- [17] H. Georgieva, V. Serbezov, Mathematical model of aircraft ground dynamics, in: Proceedings of the International Conference on Military Technologies (ICMT), Brno, Czech Republic, 2017, pp. 514 – 519.
- [18] E. Sadien, C. Roos, A. Birouche, C. Grimault, L. E. Romana, J. Boada-Bauxell, M. Basset, Control design oriented modeling of an on-ground aircraft, in: Proceedings of the European Control Conference, Limassol, Cyprus, 2018, pp. 2757 – 2762.
- [19] R. F. Stengel, Flight Dynamics, Princeton University Press, 2015.
- [20] H. Pacejka, Tire and Vehicle Dynamics, 3rd Edition, Elsevier, 2016.
- [21] J. Reimpell, H. Stoll, J. W. Betzler, The automotive chassis: Engineering principles, SAE International, 2001.
- [22] R. Rajamani, Chapter 13: Lateral and longitudinal tire forces, in: Vehicle Dynamics and Control, Springer, 2012, pp. 355 – 396.
- [23] R. Brach, M. Brach, The tire-force ellipse (friction ellipse) and tire characteristics, Tech. Rep. 2011-01-0094, SAE International (2011).
- [24] D. J. Mitchell, Frictional and retarding forces on aircraft tyres part IV: Estimation of effects of yaw, Tech. Rep. 86016a, ESDU (2006).
- [25] J. Duprez, Automatisation du pilotage au sol pour la navigation aéroportuaire, Ph.D. thesis, Université Toulouse III – Paul Sabatier, Toulouse, France (2004).
- [26] P. Goupil, J. Boada-Bauxell, A. Marcos, E. Cortet, M. Kerr, H. Costa, Airbus efforts towards advanced real-time fault diagnosis and fault tolerant control, in: Proceedings of the 19th IFAC World Congress, Cape Town, South Africa, 2014, pp. 3471 – 3476.
- [27] J.-M. Biannic, J. Boada-Bauxell, A civilian aircraft landing challenge, Tech. rep., ONERA and Airbus, <http://w3.onera.fr/smac/> (2016).
- [28] A. Isidori, Nonlinear Control Systems, Springer, 1995.
- [29] T. I. Fossen, T. A. Johansen, T. Perez, Chapter 7: A survey of control allocation methods for underwater vehicles, in: A. V. Inzartsev (Ed.), Underwater Vehicles, InTech, 2008, pp. 109 – 128.
- [30] D. Enns, Control allocation approaches, in: Proceedings of the AIAA Guidance, Navigation, and Control Conference, Boston, USA, 1998, pp. 98 – 108.
- [31] W. C. Durham, Constrained control allocation, Journal of Guidance, Control and Dynamics 16 (4) (1993) 717 – 725.

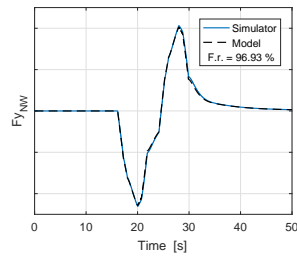
- [32] J. B. Davidson, F. J. Lallman, W. T. Bundick, Integrated reconfigurable control allocation, in: Proceedings of the AIAA Guidance, Navigation, and Control Conference, Montreal, Canada, 2001.
- [33] O. Härkegård, Backstepping and control allocation with applications to flight control, Ph.D. thesis, Linköping University, Linköping, Sweden (2003).
- [34] K. A. Bordignon, Constrained control allocation for systems with redundant control effectors, Ph.D. thesis, Virginia Polytechnic Institute and State University, Blacksburg, USA (1996).
- [35] J. A. M. Petersen, M. Bodson, Constrained quadratic programming techniques for control allocation, *IEEE Transactions on Control Systems Technology* 14 (1) (2006) 91 – 98.
- [36] J. J. Burken, P. Lu, Z. Wu, C. Bahm, Two reconfigurable flight-control design methods: Robust servomechanism and control allocation, *Journal of Guidance, Control and Dynamics* 24 (3) (2001) 482 – 493.
- [37] P. Lötstedt, Solving the minimal least squares problem subject to bounds on the variables, *BIT Numerical Mathematics* 24 (1984) 206 – 224.
- [38] M. Bodson, Evaluation of optimization methods for control allocation, *Journal of Guidance, Control and Dynamics* 25 (4) (2002) 703 – 711.
- [39] A. Zhang, Y. Wang, Z. Zhang, H. R. Karimi, Robust control allocation for spacecraft attitude stabilization under actuator faults and uncertainty, *Mathematical Problems in Engineering* (2014) 1 – 12.
- [40] Q. Shen, D. Wang, S. Zhu, E. K. Poh, Robust control allocation for spacecraft attitude tracking under actuator faults, *IEEE Transactions on Control Systems Technology* 25 (3) (2017) 1068–1075.
- [41] D. Buzorgnia, A. Khaki-Sedigh, Constrained dynamic control allocation in the presence of singularity and infeasible solutions, [arXiv:1607.05209](https://arxiv.org/abs/1607.05209).
- [42] A. K. Naskar, S. Patra, S. Sen, New control allocation algorithms in fixed point framework for overactuated systems with actuator saturation, *International Journal of Control* 90 (2) (2017) 348 – 356.
- [43] J. D. Bošković, R. K. Mehra, Control allocation in overactuated aircraft under position and rate limiting, in: Proceedings of the American Control Conference, Anchorage, USA, 2002, pp. 791 – 796.
- [44] Y. Chen, J. Wang, Fast and global optimal energy-efficient control allocation with applications to over-actuated electric ground vehicles, *IEEE Transactions on Control Systems Technology* 20 (5) (2012) 1202 – 1211.

- [45] L. Zaccarian, Dynamic allocation for input redundant control systems, *Automatica* 45 (6) (2009) 1431 – 1438.
- [46] Y. Ikeda, M. Hood, An application of L1 optimization to control allocation, in: *Proceedings of the AIAA Guidance, Navigation, and Control Conference*, Denver, USA, 2000.

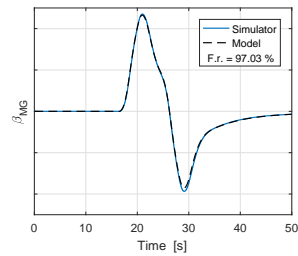
A Time responses for maneuver 1



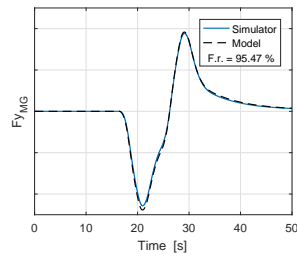
(a) Nose-wheel sideslip angle



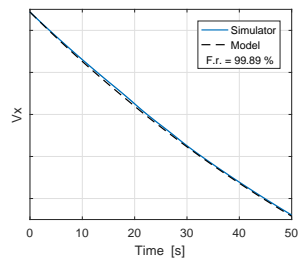
(b) Nose-wheel lateral force



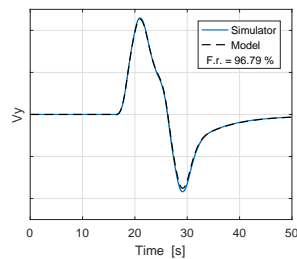
(c) Main gear wheel sideslip angle



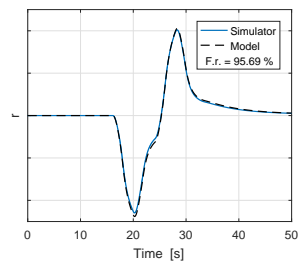
(d) Main gear wheel lateral force



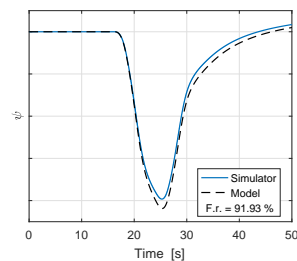
(e) Longitudinal speed



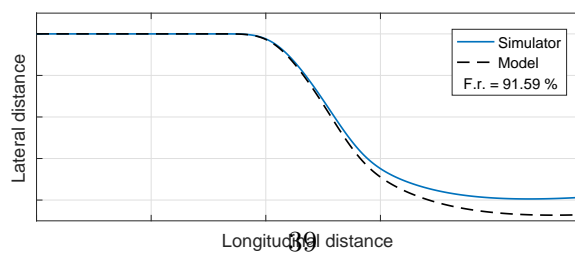
(f) Lateral speed



(g) Yaw rate



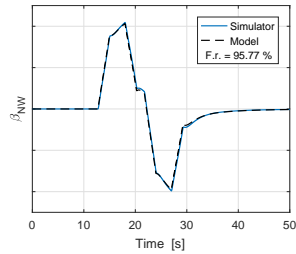
(h) Heading



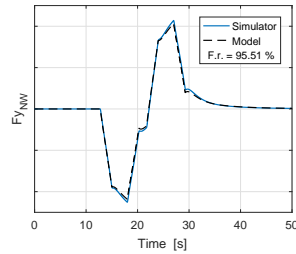
(i) Trajectory

Figure 13: Maneuver 1 – rudder pedal order at high speed

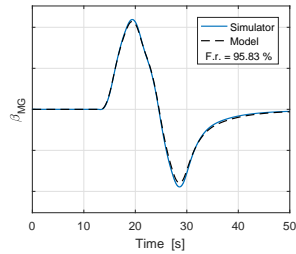
B Time responses for maneuver 3



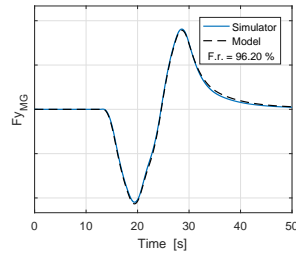
(a) Nose-wheel sideslip angle



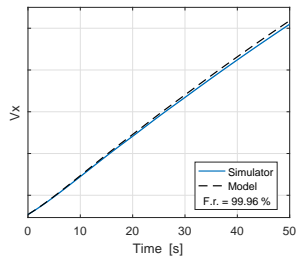
(b) Nose-wheel lateral force



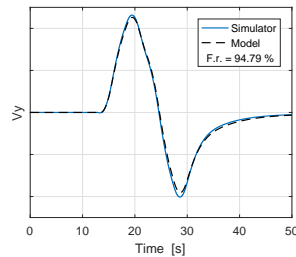
(c) Main gear wheel sideslip angle



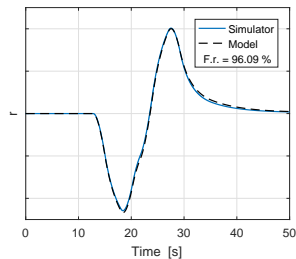
(d) Main gear wheel lateral force



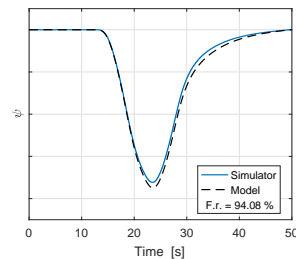
(e) Longitudinal speed



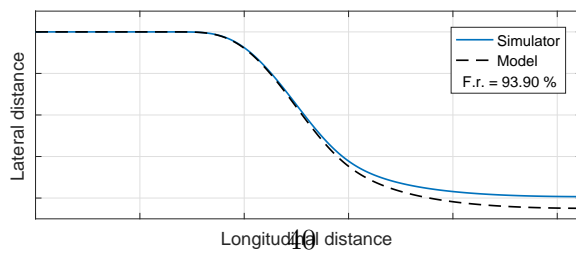
(f) Lateral speed



(g) Yaw rate



(h) Heading



(i) Trajectory

Figure 14: Maneuver 3 – handwheel order at low speed

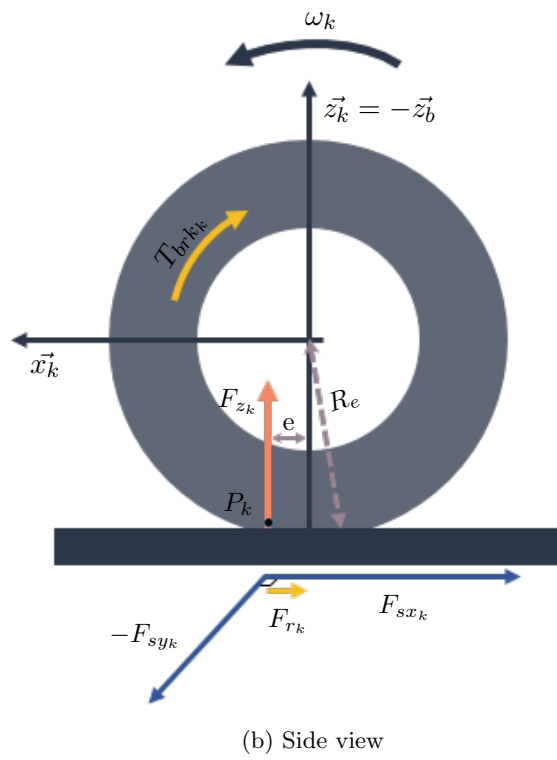
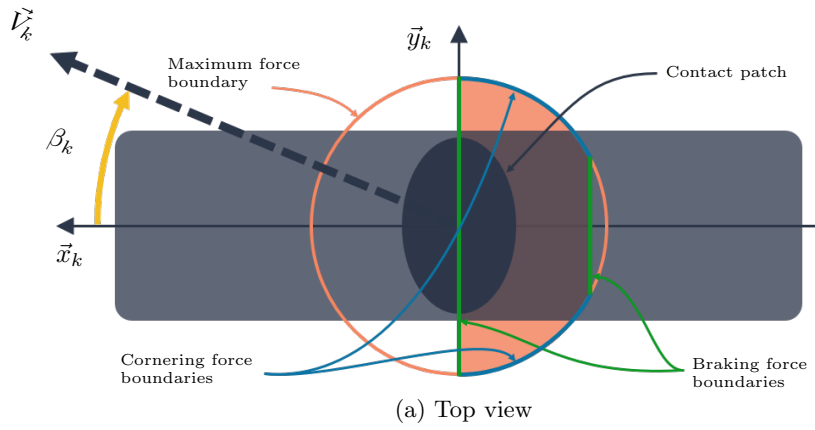


Figure 2: Wheel reference system \mathcal{R}_k and forces/moments

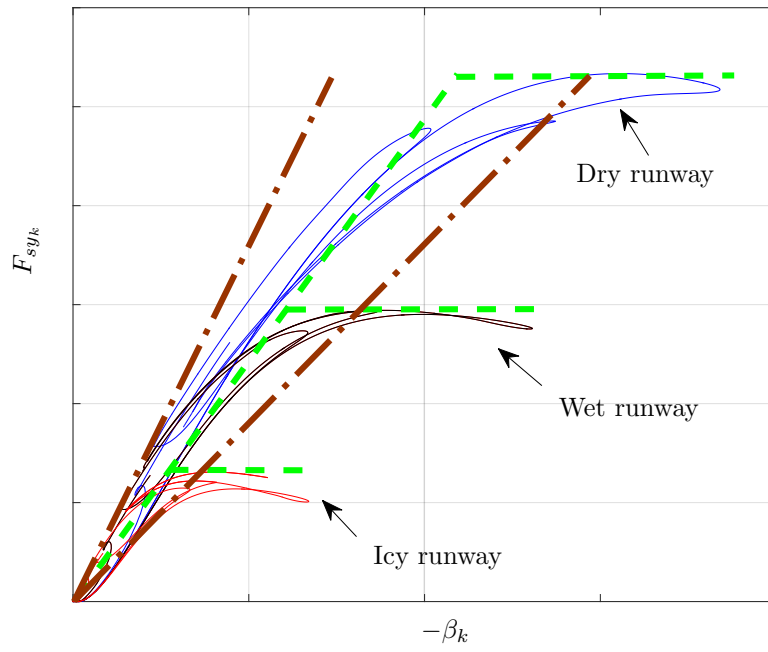
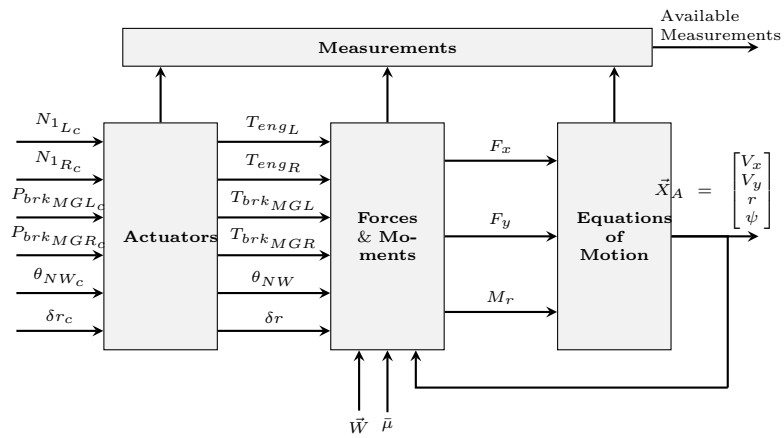
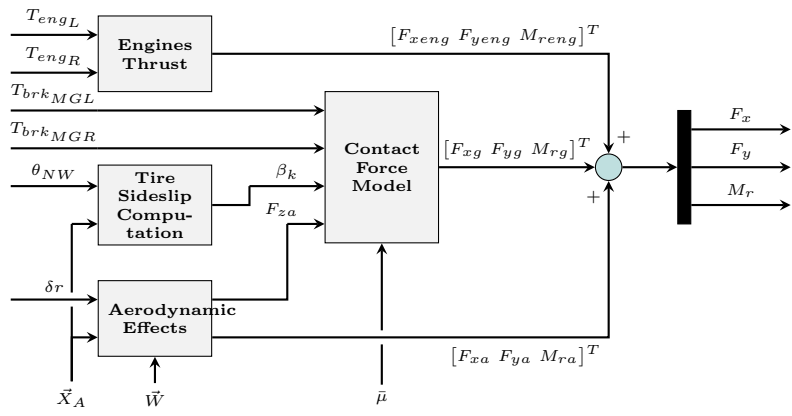


Figure 3: Lateral slip model proposed in [15]

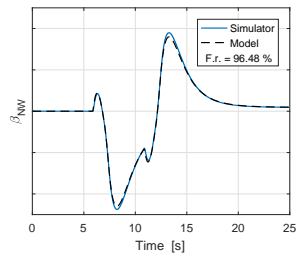


(a) Global architecture

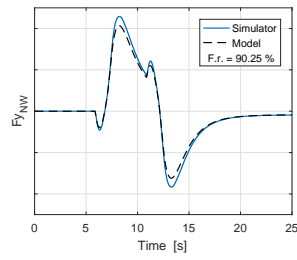


(b) Forces and moments computation

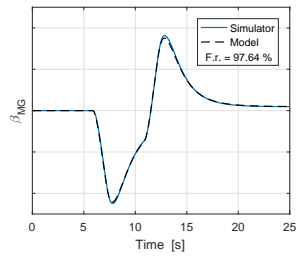
Figure 4: Proposed on-ground aircraft model



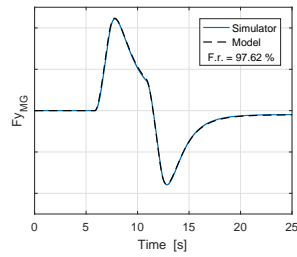
(a) Nose-wheel sideslip angle



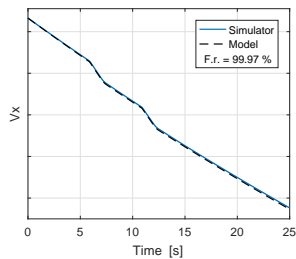
(b) Nose-wheel lateral force



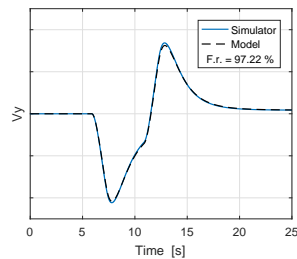
(c) Main gear wheel sideslip angle



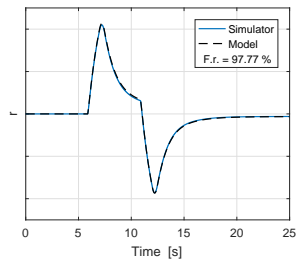
(d) Main gear wheel lateral force



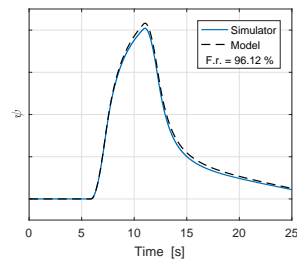
(e) Longitudinal speed



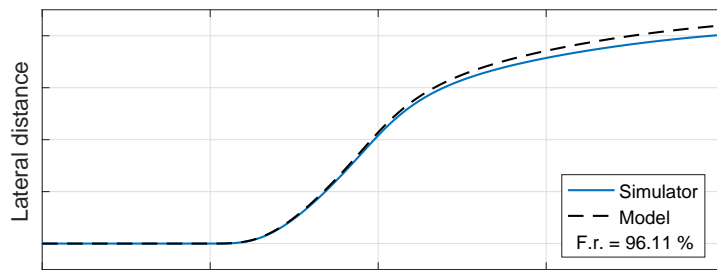
(f) Lateral speed



(g) Yaw rate



(h) Heading



(i) Trajectory

Figure 5: Maneuver 2 – differential braking order at medium speed

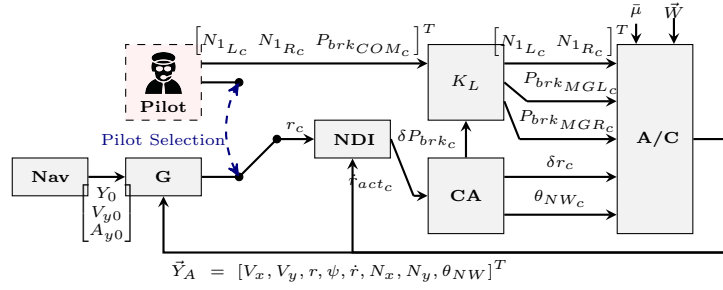


Figure 6: Lateral ground control architecture

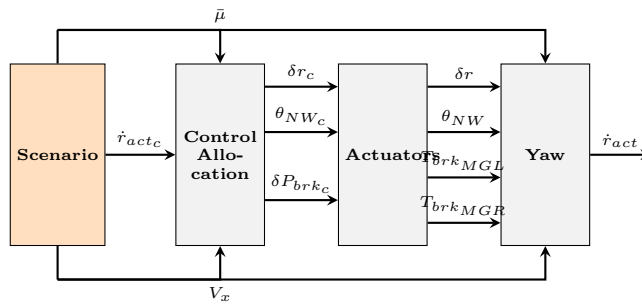


Figure 7: Benchmark architecture

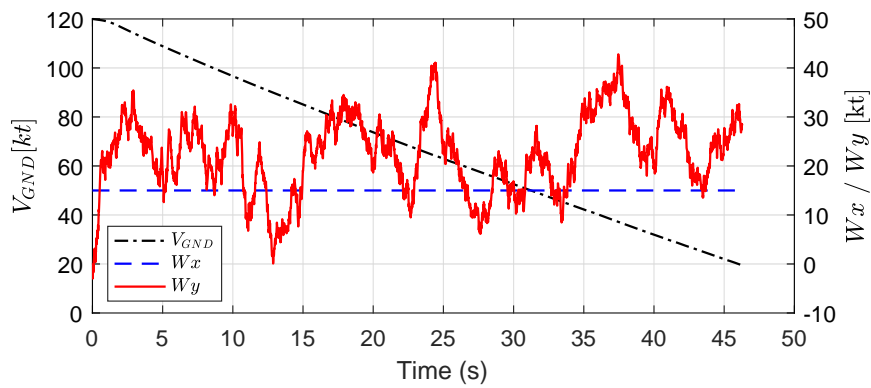


Figure 8: Ground speed V_{GND} and wind profiles

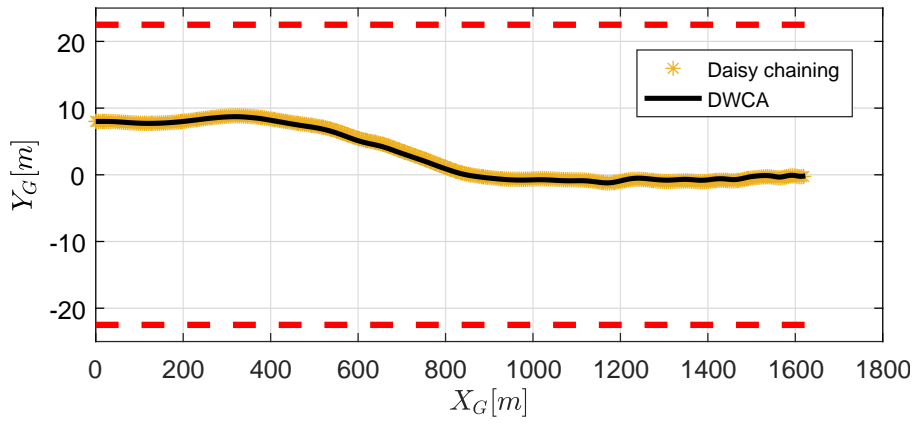


Figure 9: Trajectory and runway limits (in dashed red)

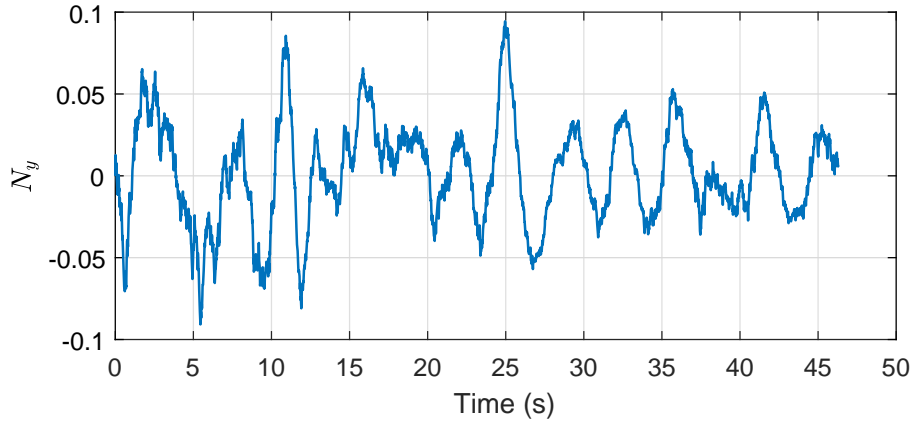


Figure 10: Lateral load factor N_y for the DWCA

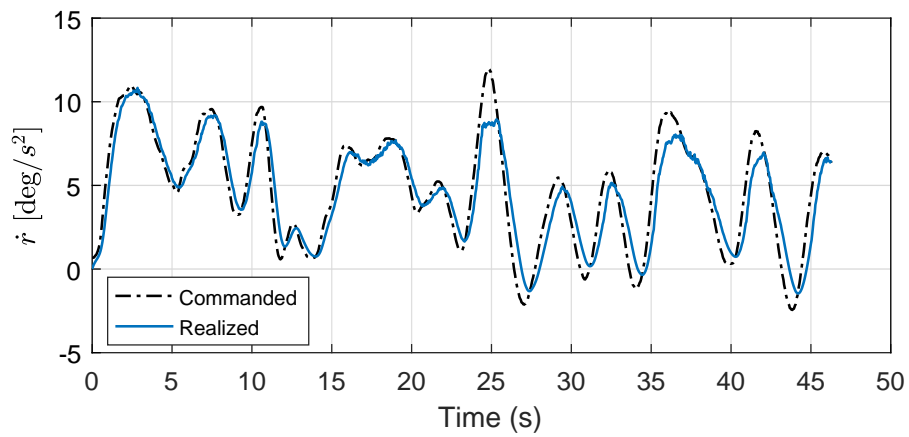
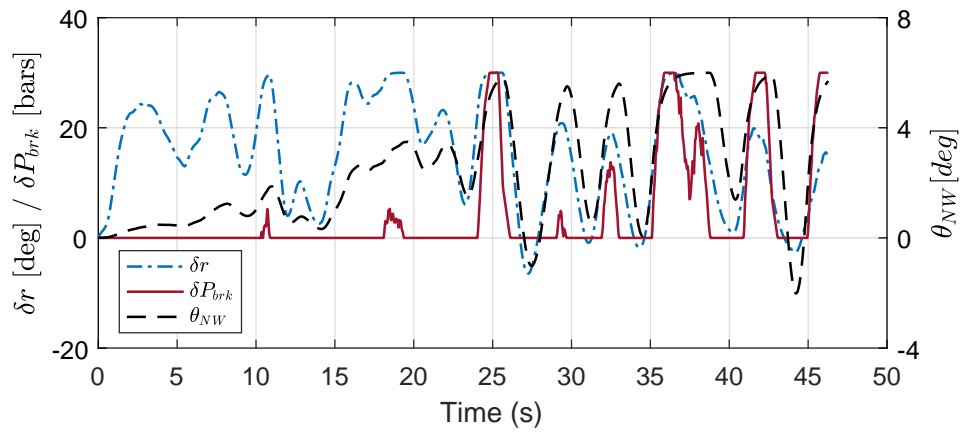
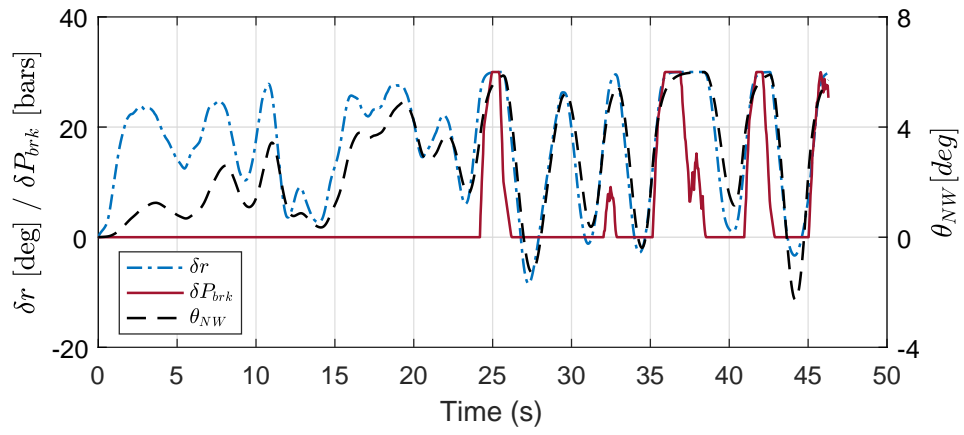


Figure 11: Commanded and realized virtual controls for the DWCA



(a) Daisy chaining



(b) DWCA

Figure 12: Actuator deflections